ATLAS Note
ANA-HDBS-2019-08-INT1
4th January 2021
Draft version 0.1

Search for heavy resonances decaying to 4ℓ final states in association with missing transverse energy in pp collisions at $\sqrt{s} = 13$ TeV with the ATLAS detector

Abdualazem Fadol[a,b,c], Humphry Tlou[a], Onesimo Mtintsilana[a], Xifeng Ruan[a], Yaquan Fang[b,c], Theodota Lagouri[d], Bruce Mellado[a], Xiaohu Sun[e]

[a] *University of the Witwatersrand*
[b] *Institute of High Energy Physics*
[c] *University of Chinese Academy of Sciences*
[d] *University of Tarapacá*
[e] *University of Manchester*

Search for the presence of a new heavy boson produced via gluon-gluon fusion in association with missing transverse energy in the four-lepton channel. The search uses the data at a centre-of-mass energy of 13 TeV collected by the ATLAS detector in the period between 2015-2018 at the Large Hadron Collider. The resonance decays to lighter Higgs-like scalar H and CP-even scalar S bosons. The H decays into 4ℓ (ℓ could be either e or μ) through ZZ bosons. The S decays to a pair of Standard Model neutrinos. The discovery of the Standard Model Higgs boson imposes questions as to whether there is physics beyond the Standard Model or not. The multilepton and the rich missing transverse energy on the final states give rise to activities of Physics Beyond the Standard Model in which we investigate in this search. An AZH model within the 2HDM framework is also examined in the similar event topology.

Contents

0 Changes and summary

0.1 Changes

V0.1 First version for the Editorial Board request.

0.2 Target

0.3 Summary

List of contributions

Abdualazem Fadol	Main analysis, contact, editor of the note, optimization, signal/background parametrisation, systematics, statistics.
Humphry Tlou	Cutflow cross-check, MET performance, and background modelling
Onesimo Mtintsilana	Cutflow cross-check and signal modelling
Xifeng Ruan	Editor, contact, modelling, optimization, signal/background parametrisation, statistics, systematics
Yaquan Fang	Author's contribution.
Theodota Lagouri	General high mass analysis.
Bruce Mellado	Model development of the $R \to SH \to 4\ell + X$ models and supervisor.
Xiaohu Sun	Model development of $A \to ZH \to 4\ell + X$ modelling.

1 Introduction

A new boson was discovered in 2012 by both ATLAS and CMS experiments [1, 2]. Its properties are compatible with the Higgs boson that proposed by the Standard model (SM) [3–6]. However, there are still questions that the SM has not answered. For example, the dark matter, neutrino masses and mixing, Hierarchy problem, and strong CP-problem [7–9]. Also, whether the new particle unique in nature or one of the Higgs sector proposed by the tow-Higgs-Doublet (2HDM) [10].

The 4ℓ decay channel played a significant role in the discovery of Higgs boson and the measurement of its properties. The search on this channel relies on a very clean signature in which the final state has a low signal-to-background ratio. The four-lepton final state in association with missing transverse energy is never examined in the ATLAS experiment. Therefore, in this analysis the production of heavy resonances via gluon-fusion in association with missing transverse energy is investigated. The heavy resonances, m_H, assumed to decay to $\ell^+\ell^-\ell^+\ell^+$ final state through the decay of a pair of Z bosons, where ℓ could be an electron or a muon. The search focuses on the high mass region of the heavy bosons where the four-lepton invariant mass is above 200 GeV.

This analysis uses proton-proton collision data at a centre-of-mass energy of 13 TeV, and integrated luminosity of 139.0 fb^{-1}collected by the ATLAS detector on 2015-2018 period at the Large Hadron Collider (LHC). The data is interpreted in terms of $R \to SH \to 4\ell + E_{\mathrm{T}}^{\mathrm{miss}}$ [11], and $A \to Z(\text{inclusive})H(ZZ \to 4\ell)$ [12] models. Feynman diagram in Figure (a) shows the first model where R is a scalar boson, and it decays to two lighter scalar bosons S and H. The S decays to SM neutrinos (thereof refereed to it as $E_{\mathrm{T}}^{\mathrm{miss}}$ here), and H decays to four leptons. To control the quantity of the missing transverse energy, the S mass is fixed to 160 GeV and scan through the R, and H masses. To explore regions with jet activities, the model in Figure (b) is introduced. A in this model is a CP-odd scalar which decays to a CP-even scalar H, and Z boson. The Z boson decays to a pair of SM neutrinos, and H decays to 4-lepton final state.

The note is organised as follows: Section 2 describes the data and Monte Carlo (MC) samples, followed by event and object selection Section 3. Section 4 describes the analysis strategy and Section 5 illustrates the background estimation. The signal and background parametrisation are discussed in Section 6. The experimental and theoretical systematic uncertainties are demonstrated in Section 7. The results are discussed in section 8 and a conclusion is given in Section 9.

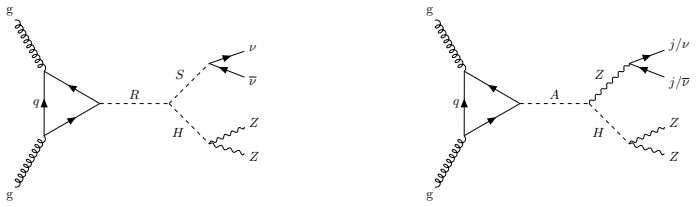

(a) (b)

Figure 1: Feynman diagrams represent the production of heavy bosons via gloun-fusion (a) $R \to SH \to 4\ell + E_{\mathrm{T}}^{\mathrm{miss}}$ and (b) $A \to Z(\text{inclusive})H(ZZ \to 4\ell)$ models.

2 Data and Monte Carlo samples

2.1 Data

The dataset used in this analysis consists of proton-proton collisions at a centre-of-mass energy of 13 TeV, recorded by the ATLAS detector at the LHC in 2015 to 2018. Requirements to ensure the quality of beam conditions, detector performance and data are imposed [13–15], as well as additional event cleaning criteria described in Section 8. [1] After application of these criteria, the dataset corresponds to a total integrated luminosity of 139.0 fb^{-1}.

2.2 Background samples

2.3 Signal samples

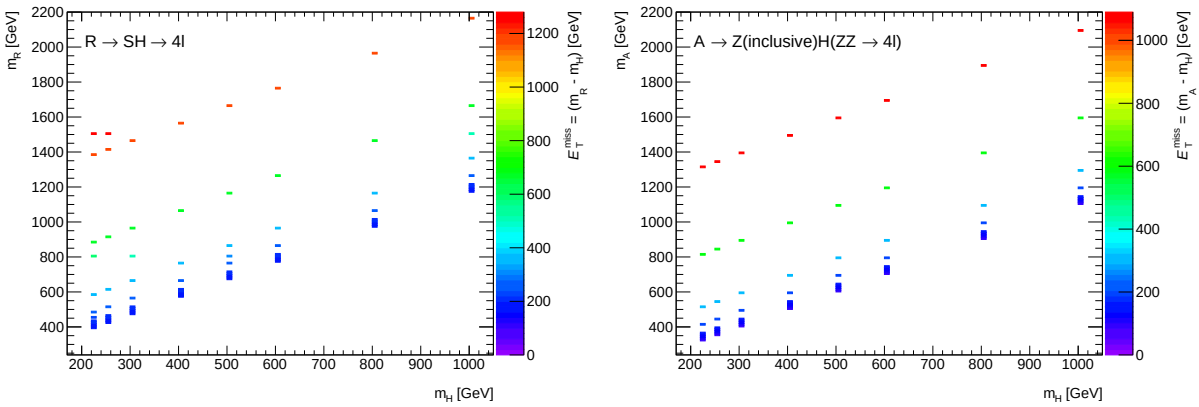

(a) (b)

Figure 2: Two-dimensional plots showing the $E_{\mathrm{T}}^{\mathrm{miss}}$ content of the (a) $R \to SH \to 4\ell + E_{\mathrm{T}}^{\mathrm{miss}}$ and (b) $A \to Z(\text{inclusive})H(ZZ \to 4\ell)$ models. The missing transverse energy is represented by the z-axis as $m_R - m_H$ or $m_A - m_H$.

[1] For the 2015 dataset:
`GoodRunsLists/data15_13TeV/20170619/data15_13TeV.periodAllYear_DetStatus-v89-pro21-02_Unknown_PHYS_StandardGRL_All_Good_25ns.xml`.
For the 2016 dataset:
`GoodRunsLists/data16_13TeV/20180129/data16_13TeV.periodAllYear_DetStatus-v89-pro21-01_DQDefects-00-02-04_PHYS_StandardGRL_All_Good_25ns.xml`.
For the 2017 dataset:
`GoodRunsLists/data17_13TeV/20180619/data17_13TeV.periodAllYear_DetStatus-v99-pro22-01_Unknown_PHYS_StandardGRL_All_Good_25ns_Triggerno17e33prim.xml`.
For the 2018 dataset:
`GoodRunsLists/data18_13TeV/20190219/data18_13TeV.periodAllYear_DetStatus-v102-pro22-04_Unknown_PHYS_StandardGRL_All_Good_25ns_Triggerno17e33prim.xml`.

3 Event and object selection

3.1 Object definitions

3.1.1 Electrons

3.1.2 Muons

3.1.3 Jets

3.1.4 Overlap removal

3.1.5 Missing transverse momentum

3.2 Event selection

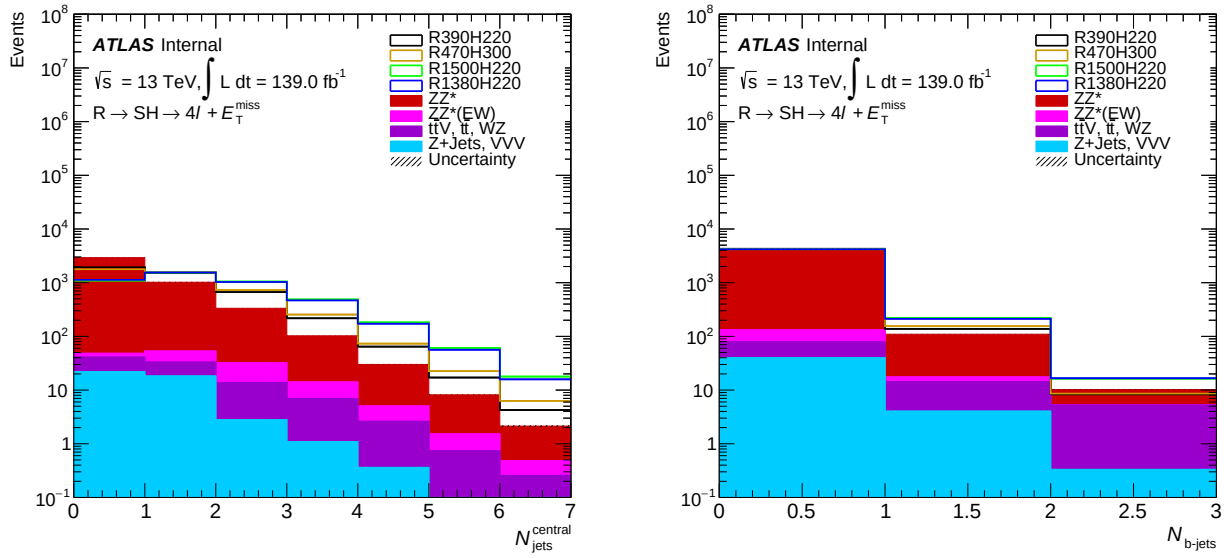

(a) (b)

Figure 3: Distribution for the $R \rightarrow SH \rightarrow 4\ell + E_{\mathrm{T}}^{\mathrm{miss}}$ signal comparing to the different background components of the (a) Number of central jets, (b) Number of b-tagged jets. Each signal is normalised to the total number of background.

4 Analysis strategy

After the pre-selection described in Section 3, an additional selection depending on the signal model is applied. This section discusses the different selection used in the optimisation. The optimisation is quantified by using the following significance formula:

$$Z = \frac{s}{\sqrt{k \cdot b}}, \tag{1}$$

where s and b represent the signal and background events, respectively. Since the signal is above 200 GeV, the background is considered above 200 GeV. k is a fraction applied on the background to consider only the background under the signal peak. For instance, k for the $(m_R, m_H) = (390, 220)$ GeV signal is 20.3%, it is the ratio between events in $m_{4\ell}[210 - 230]$ and the entire $m_{4\ell}$ region greater than 200 GeV. Each signal model has different optimisation strategy as showing below.

4.1 $R \rightarrow SH \rightarrow 4\ell + E_{\mathrm{T}}^{\mathrm{miss}}$ signal optimisation

For simplicity, four signal samples are selected to compare their shapes with SM backgrounds for some kinematic distributions. Two signals with lower $E_{\mathrm{T}}^{\mathrm{miss}}$ around 50 GeV, and the other with high $E_{\mathrm{T}}^{\mathrm{miss}}$ above 600 GeV, see Figure 4(c). Figure 3 shows number of jets and b-jets, and Figure 4 shows the 4-lepton

Table 1: The expected yields for the $(m_R, m_H) = (390, 220)$ GeV signal mass point, and the total background calculated from the state-of-the-art MC simulation with an integrated luminosity of 139.0 fb^{-1}. The uncertainties included on the table are statistical uncertainty only. Expected events at 4ℓ cut are after the pre-selection discussed on Section 3. $E_{\mathrm{T}}^{\mathrm{miss}}$ significance is represented by metSig on the table.

	$(m_R, m_H) = (390, 220)$ GeV	$qq \to ZZ^*$	$gg \to ZZ^*$	$qq \to ZZ^*$ (EW)	$t\bar{t}V$	VVV	Z + jets	WZ	$t\bar{t}$	Total background
4ℓ	64.29±0.27	2516.52±4.50	348.96±0.71	32.85±0.28	8.60±0.05	19.04±0.11	10.35±8.28	5.12±0.34	2.68±0.20	2944.13±14.48
b-veto	62.15±0.27	2451.45±4.47	341.64±0.70	30.67±0.27	2.14±0.02	18.48±0.11	10.35±8.28	4.96±0.33	1.77±0.15	2861.46±14.34
$N_{\mathrm{Jets}}^{\mathrm{Central}} = 0$	28.17±0.18	1625.63±3.87	212.93±0.56	3.10±0.11	0.41±0.01	9.40±0.07	9.69±8.27	2.85±0.26	0.78±0.08	1864.79±13.23
$p_{\mathrm{T}}^{4\ell} > 30$ & metSig > 2.0	14.98±0.13	82.73±0.94	21.12±0.18	0.51±0.03	0.33±0.01	7.22±0.07	0.32±0.32	1.69±0.19	0.53±0.07	114.44±1.80
$p_{\mathrm{T}}^{4\ell} > 15$ & metSig > 1.5	21.86±0.16	258.04±1.74	58.30±0.29	0.99±0.04	0.37±0.01	8.17±0.07	1.82±1.54	2.13±0.21	0.65±0.07	330.47±3.99
$N_{\mathrm{Jets}}^{\mathrm{Central}} \geq 1$	33.99±0.20	825.82±2.24	128.71±0.43	27.56±0.25	1.73±0.02	9.08±0.08	0.66±0.35	2.11±0.21	0.99±0.12	996.67±3.71
$p_{\mathrm{T}}^{4\ell} > 10$ & metSig > 3.5	12.86±0.12	10.46±0.23	2.25±0.06	0.30±0.02	0.93±0.02	4.68±0.06	0.01±0.01	0.76±0.13	0.63±0.11	20.02±0.63
$p_{\mathrm{T}}^{4\ell} > 0$ & metSig > 2.5	21.02±0.16	51.55±0.66	10.66±0.13	1.35±0.05	1.25±0.02	6.19±0.07	0.01±0.01	1.09±0.15	0.75±0.11	72.83±1.19

Table 2: Summary of the $R \to SH \to 4\ell + E_{\mathrm{T}}^{\mathrm{miss}}$ categories, significance calculated using equation 1 and their representation.

$R \to SH \to 4\ell + E_{\mathrm{T}}^{\mathrm{miss}}$ categories	Representation	Z
$N_{\mathrm{Jets}}^{\mathrm{Central}} = 0$ & $p_{\mathrm{T}}^{4\ell} > 30.0$ & metSig > 2.0	High-$E_{\mathrm{T}}^{\mathrm{miss}}$ & $N_{\mathrm{jets}}^{\mathrm{Central}} = 0$	3.11
$N_{\mathrm{Jets}}^{\mathrm{Central}} = 0$ & $p_{\mathrm{T}}^{4\ell} > 15.0$ & metSig > 1.5	Low-$E_{\mathrm{T}}^{\mathrm{miss}}$ & $N_{\mathrm{jets}}^{\mathrm{Central}} = 0$	1.04
$N_{\mathrm{Jets}}^{\mathrm{Central}} \geq 1$ & $p_{\mathrm{T}}^{4\ell} > 10.0$ & metSig > 3.5	High-$E_{\mathrm{T}}^{\mathrm{miss}}$ & $N_{\mathrm{jets}}^{\mathrm{Central}} \geq 1$	6.39
$N_{\mathrm{Jets}}^{\mathrm{Central}} \geq 1$ & $p_{\mathrm{T}}^{4\ell} > 0$ & metSig > 2.5	Low-$E_{\mathrm{T}}^{\mathrm{miss}}$ & $N_{\mathrm{jets}}^{\mathrm{Central}} \geq 1$	2.49
Combined significance		7.60

invariant mass, 4-lepton momentum, $E_{\mathrm{T}}^{\mathrm{miss}}$ and $E_{\mathrm{T}}^{\mathrm{miss}}$ significance. The event-based $E_{\mathrm{T}}^{\mathrm{miss}}$ significance is defined as:

$$E_{\mathrm{T}}^{\mathrm{miss}}\text{significance} = \frac{E_{\mathrm{T}}^{\mathrm{miss}}}{\sqrt{\sum E_{\mathrm{T}}}}. \tag{2}$$

The $E_{\mathrm{T}}^{\mathrm{miss}}$ significance is used on the optimisation instead of the $E_{\mathrm{T}}^{\mathrm{miss}}$ and object-based $E_{\mathrm{T}}^{\mathrm{miss}}$ significance [16], because it gives better significance, see Appendix will be added soon. The zero central jet bin contains most of the background, and it dropped to $\sim$ 66% in the one central jet bin. After the pre-selection, we veto b-tagged jets to suppress $t\bar{t}$ related background. Then categorise events into zero and at least one central jet. Figure 4 shows kinematic distributions of the $m_{4\ell}$, $p_{\mathrm{T}}^{4\ell}$ and $E_{\mathrm{T}}^{\mathrm{miss}}$. The latter two employed to discriminate signal from backgrounds by doing a two-dimensional (2D) scan. The $(m_R, m_H) = (390, 220)$ GeV signal sample is used for the optimisation. Because using a sample with low $E_{\mathrm{T}}^{\mathrm{miss}}$ covers ones with high $E_{\mathrm{T}}^{\mathrm{miss}}$, see Figure 4(c), but that underestimates the high $E_{\mathrm{T}}^{\mathrm{miss}}$ sample significance. As number of SM backgrounds under the high $E_{\mathrm{T}}^{\mathrm{miss}}$ peak is less than that of the low $E_{\mathrm{T}}^{\mathrm{miss}}$. For the zero central jet category, a 2D scan is performed for $E_{\mathrm{T}}^{\mathrm{miss}}$ significance and $p_{\mathrm{T}}^{4\ell}$. Two optimal points are found at $E_{\mathrm{T}}^{\mathrm{miss}}$ significance >2.0 and $p_{\mathrm{T}}^{4\ell} > 30.0$ GeV with significance of 3.14, as shown in Figure 5(a). Another scan carried out at low missing transverse energy after removing the optimal points. Figure 5(b) shows the lower $E_{\mathrm{T}}^{\mathrm{miss}}$ scan results where $E_{\mathrm{T}}^{\mathrm{miss}}$ significance >1.5 and $p_{\mathrm{T}}^{4\ell} > 15.0$ GeV. The same technique is used for at least one central jet category, as shown in Figures 5(c) and 5(d). A cut-flow of the zero and at least one central jet category with their low and high $E_{\mathrm{T}}^{\mathrm{miss}}$ bin is shown in Table 1. A summary of the optimal cuts, their representation and the significance of each cut is shown in Table 2. The combined significance for all categorise is 7.60

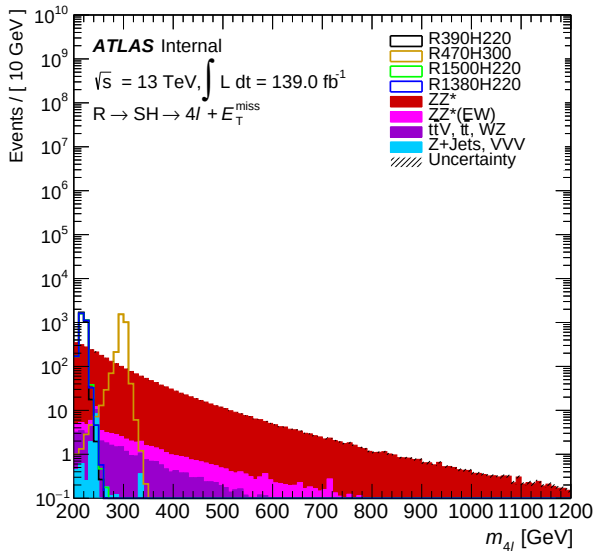

(a)

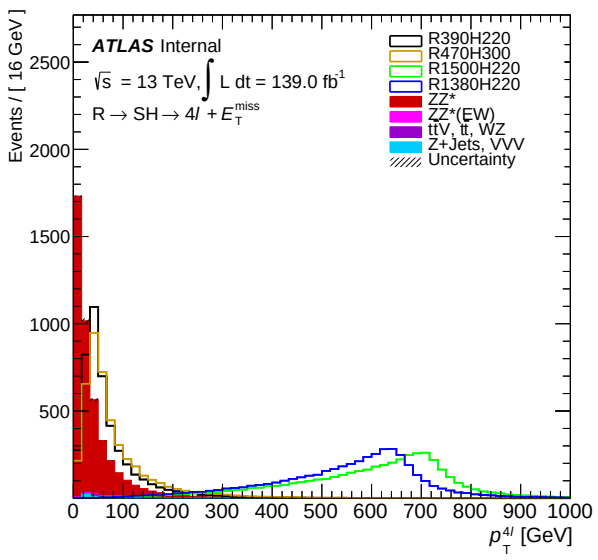

(b)

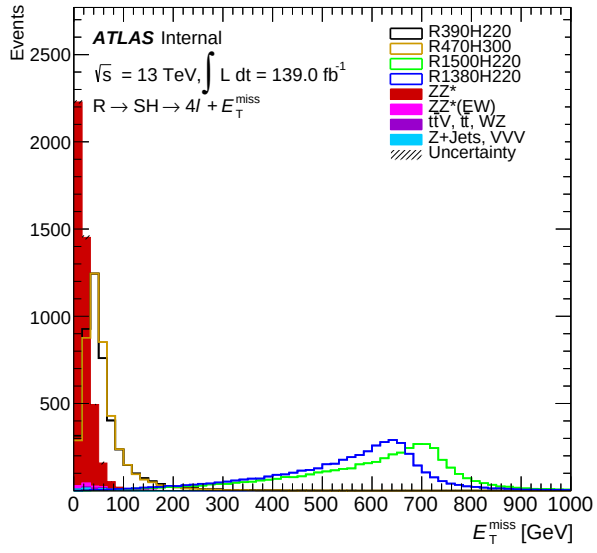

(c)

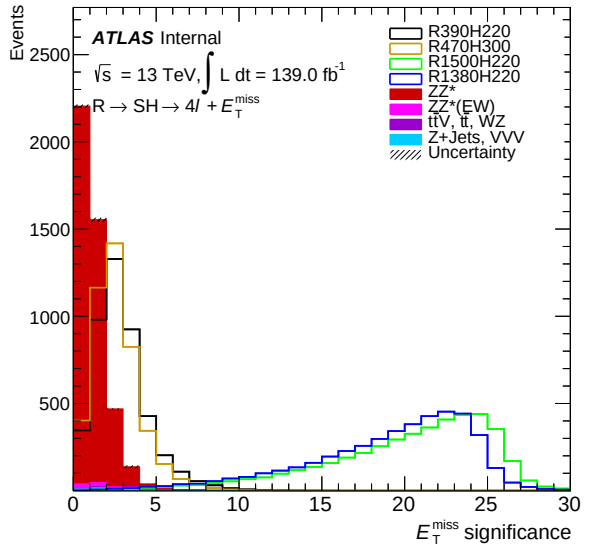

(d)

Figure 4: Distribution for the $R \rightarrow SH \rightarrow 4\ell + E_{\mathrm{T}}^{\mathrm{miss}}$ signal comparing to the different background components of the (a) Four-lepton invariant mass, (b) Four-lepton transverse momentum, (c) Missing transverse energy and (a) $E_{\mathrm{T}}^{\mathrm{miss}}$ significance. Each signal is normalised to the total number of background to get better comparison with the background.

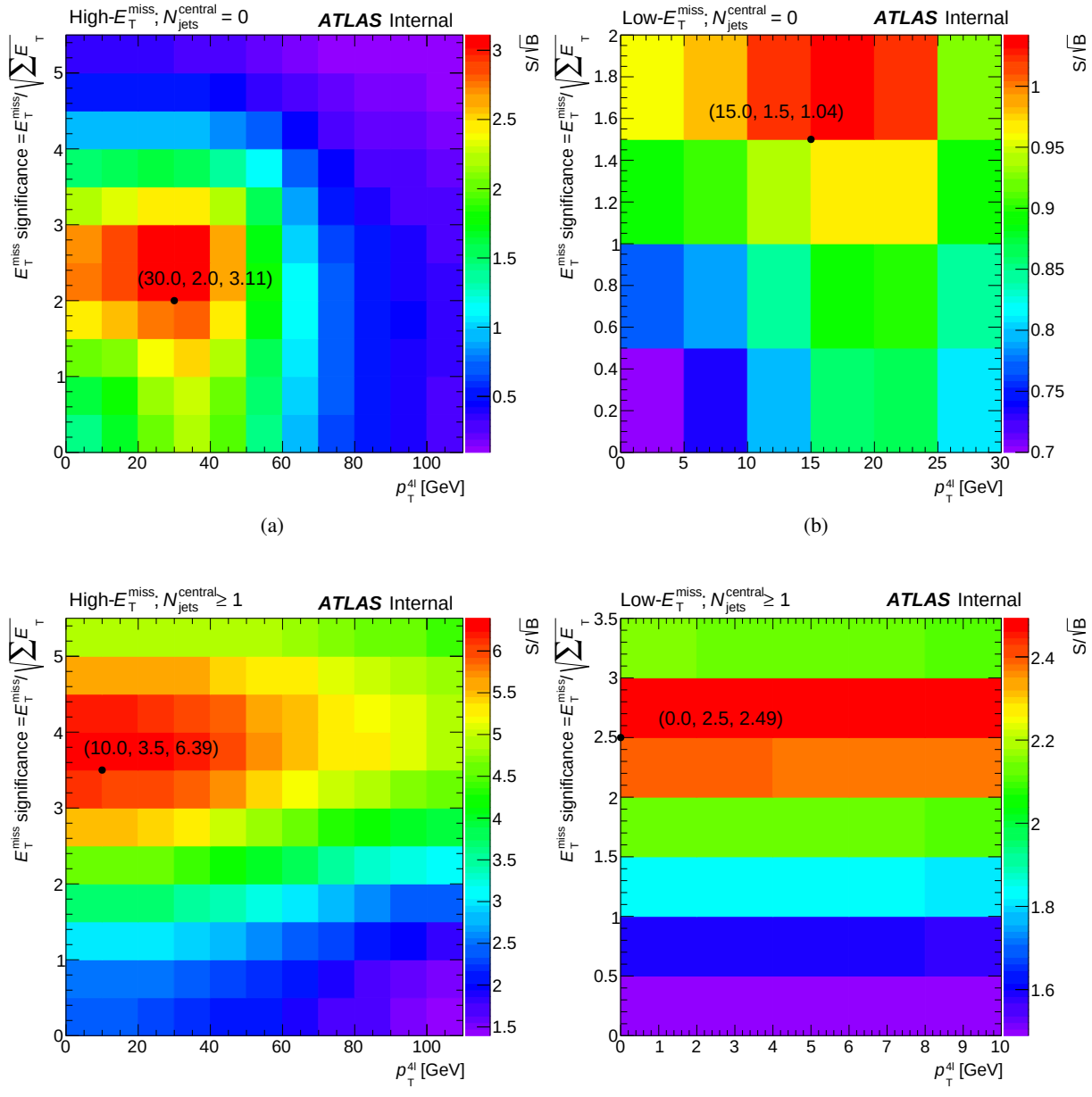

Figure 5: $R \rightarrow SH \rightarrow 4\ell + E_{\mathrm{T}}^{\mathrm{miss}}$ signal optimisation for the (a) High-$E_{\mathrm{T}}^{\mathrm{miss}}$ and $N_{\mathrm{jets}}^{\mathrm{Central}} = 0$, (b) Low-$E_{\mathrm{T}}^{\mathrm{miss}}$ and $N_{\mathrm{jets}}^{\mathrm{Central}} = 0$, (c) High-$E_{\mathrm{T}}^{\mathrm{miss}}$ and $N_{\mathrm{jets}}^{\mathrm{Central}} \geq 1$ and (d) Low-$E_{\mathrm{T}}^{\mathrm{miss}}$ and $N_{\mathrm{jets}}^{\mathrm{Central}} \geq 1$ categories.

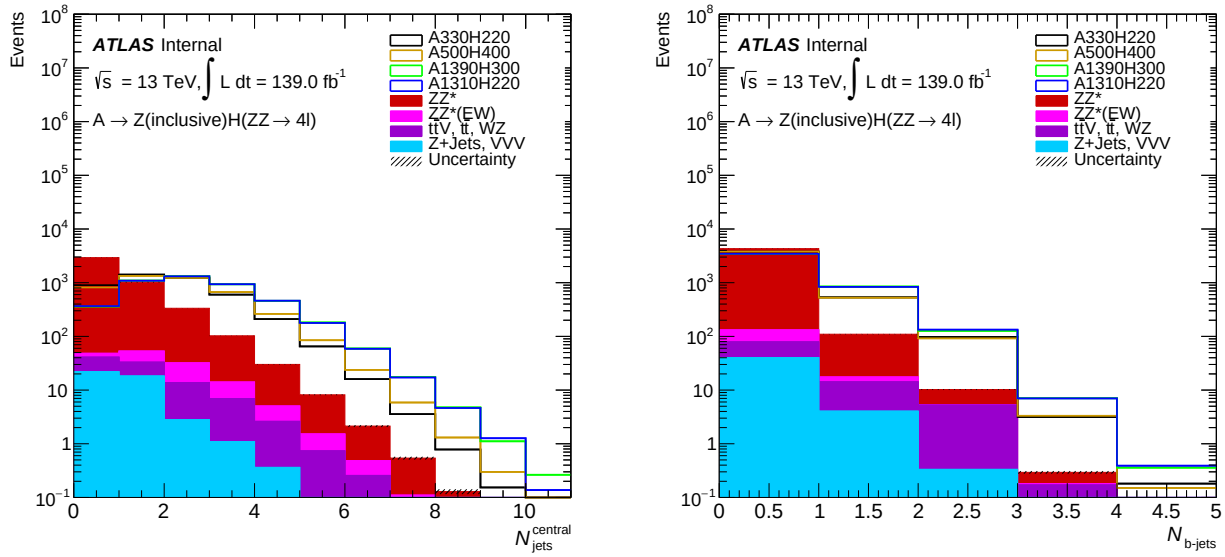

(a) (b)

Figure 6: Distribution for the $A \rightarrow Z(\text{inclusive})H(ZZ \rightarrow 4\ell)$ signal comparing to the different background components of the (a) Number of central jets and (b) Number of b-tagged jets. Each signal is normalised to the total number of SM backgrounds.

4.2 $A \rightarrow Z(\text{inclusive})H(ZZ \rightarrow 4\ell)$ signal optimisation

We keep categories from $R \rightarrow SH \rightarrow 4\ell + E_{\text{T}}^{\text{miss}}$ signal optimisation, because $p_{\text{T}}^{4\ell}$ and $E_{\text{T}}^{\text{miss}}$ significance kinematics have the same pattern as in $R \rightarrow SH \rightarrow 4\ell + E_{\text{T}}^{\text{miss}}$ model, see Figure 7. Figure 6 shows the central jets and b-jets kinematic distributions, where more jets activity is observed. The leading and sub-leading central jets kinematics are shown in Figure 8. In addition to the $E_{\text{T}}^{\text{miss}}$ categories, further categorisation is implemented. Events are required to have at least one b-jets, then at least two central jets with events inside the $m_{\text{jj}}^{\text{Central}}$ peak. Hence exactly one central jet is selected together with events outside $m_{\text{jj}}^{\text{Central}}$ peak. The remaining events are labelled as Rest category. Table 3 summarises the categories, yields and the significance calculated by equation 2 for the $A \rightarrow Z(\text{inclusive})H(ZZ \rightarrow 4\ell)$ model. The k factor used is 20.3% corresponds to the ratio of events in $m_{4\ell}[210-230]$ and $m_{4\ell}$ above 200 GeV.

Table 3: The expected yields for the $(m_A, m_H) = (330, 220)$ GeV signal mass point, and the significance calculated from the state-of-the-art MC simulation with an integrated luminosity of 139.0 fb^{-1}. The uncertainties included on the table are statistical uncertainty only. Expected events at 4ℓ cut are after the pre-selection discussed on Section 3.

	$(m_A, m_H) = (330, 220)$	$qq \rightarrow ZZ^*$	$gg \rightarrow ZZ^*$	$qq \rightarrow ZZ^*$ (EW)	$t\bar{t}V$	VVV	Z + jets	WZ	$t\bar{t}$	Z
4ℓ	60.35±0.13	2516.52±4.50	348.96±0.71	32.85±0.28	10.35±8.28	19.04±0.11	8.60±0.05	5.12±0.34	2.68±0.20	2.47
High-$E_{\text{T}}^{\text{miss}}$ & $N_{\text{jets}}^{\text{Central}} = 0$	5.61±0.04	82.73±0.94	21.12±0.18	0.51±0.03	0.32±0.32	7.22±0.07	0.33±0.01	1.69±0.19	0.53±0.07	1.16
Low-$E_{\text{T}}^{\text{miss}}$ & $N_{\text{jets}}^{\text{Central}} = 0$	2.22±0.02	175.31±1.47	37.18±0.23	0.48±0.03	1.51±1.51	0.96±0.02	0.04±0.00	0.44±0.10	0.12±0.03	0.33
High-$E_{\text{T}}^{\text{miss}}$ & $N_{\text{jets}}^{\text{Central}} \geq 1$	2.88±0.03	10.46±0.23	2.25±0.06	0.30±0.02	0.01±0.01	4.68±0.06	0.93±0.02	0.76±0.13	0.63±0.11	1.43
Low-$E_{\text{T}}^{\text{miss}}$ & $N_{\text{jets}}^{\text{Central}} \geq 1$	4.50±0.03	41.09±0.62	8.40±0.11	1.04±0.04	0.00±0.00	1.50±0.03	0.32±0.01	0.32±0.08	0.12±0.03	1.37
$N_{\text{b-jets}} \geq 1$	8.94±0.05	65.07±0.54	7.32±0.11	2.19±0.07	0.00±0.00	0.56±0.02	6.45±0.04	0.16±0.06	0.92±0.13	2.18
$N_{\text{jets}}^{\text{Central}} \geq 2$& $\lvert m_{jj}^{\text{Central}} - m_Z \rvert < 60$	10.86±0.05	113.57±0.53	18.48±0.16	3.65±0.08	0.25±0.21	0.50±0.02	0.11±0.01	0.14±0.05	0.03±0.01	2.06
$N_{\text{jets}}^{\text{Central}} = 1$ & $\lvert m_{jj}^{\text{Central}} - m_Z \rvert > 60$	12.31±0.06	526.17±2.00	80.78±0.34	8.83±0.14	0.34±0.28	1.58±0.03	0.19±0.01	0.68±0.12	0.16±0.05	1.10
Rest	13.04±0.06	1502.12±3.49	173.43±0.50	15.85±0.21	7.93±8.13	2.04±0.03	0.22±0.01	0.94±0.16	0.17±0.04	0.70

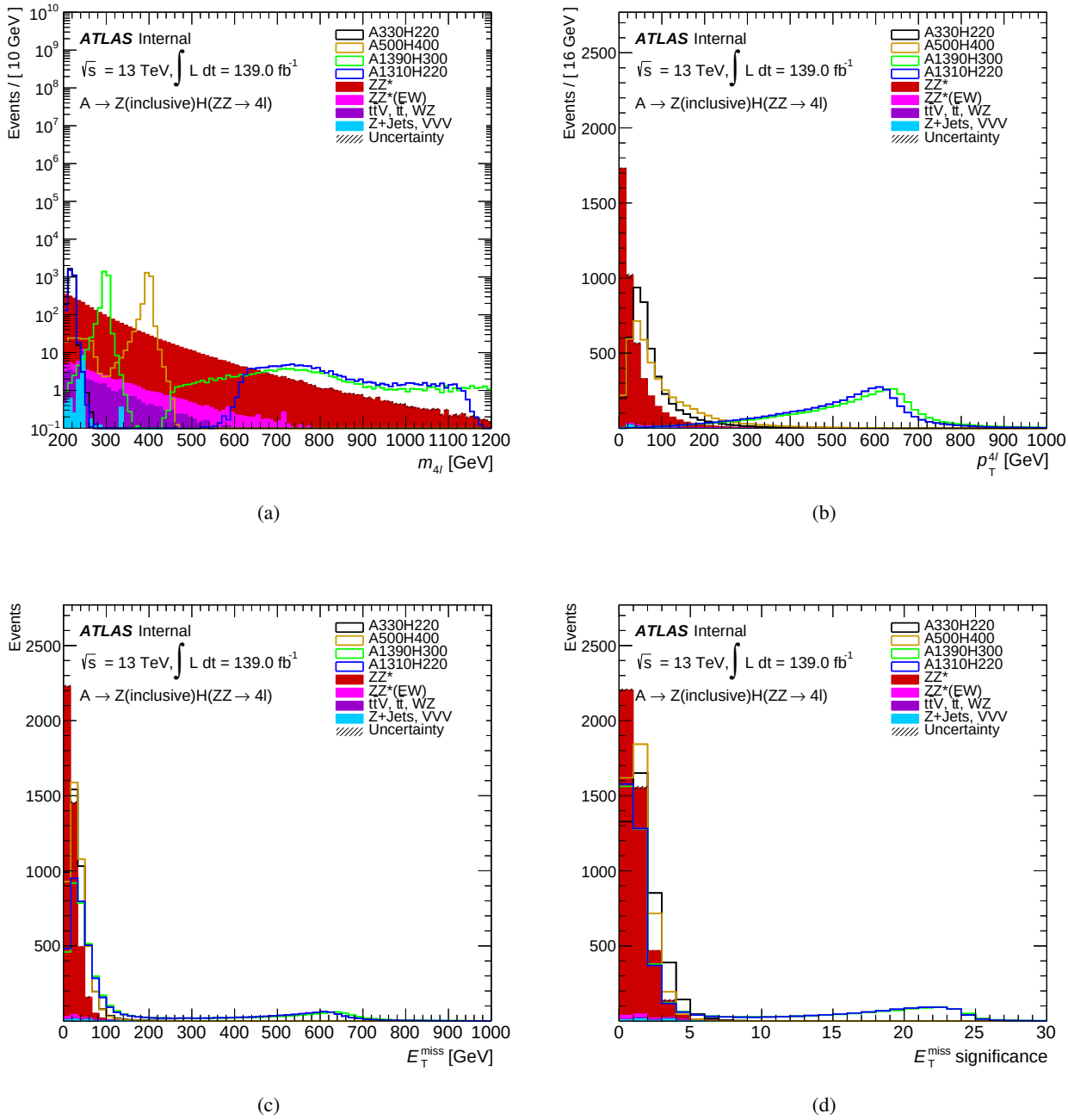

(a) (b)

(c) (d)

Figure 7: Distribution for the $A \rightarrow Z(\text{inclusive})H(ZZ \rightarrow 4\ell)$ signal comparing to the different background components of the (a) Four-lepton invariant mass, (b) Four-lepton transverse momentum, (c) Missing transverse energy and (a) $E_{\mathrm{T}}^{\mathrm{miss}}$ significance. Each signal is normalised to the total number of background.

The significance of the Low-$E_{\mathrm{T}}^{\mathrm{miss}}$ & $N_{\mathrm{jets}}^{\mathrm{Central}} = 0$ and the Rest categories are 0.33 and 0.70 respectively. So we dropped these two categorise, since they are small. The combined significance for the 6 categories of the $A \rightarrow Z(\text{inclusive})H(ZZ \rightarrow 4\ell)$ model is 3.93.

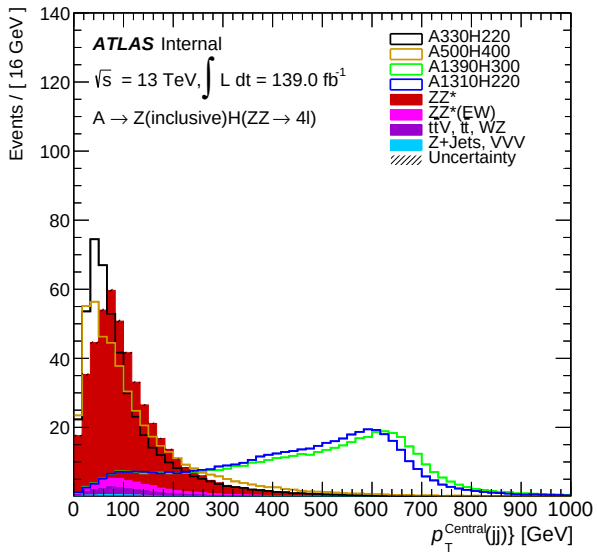

(a)

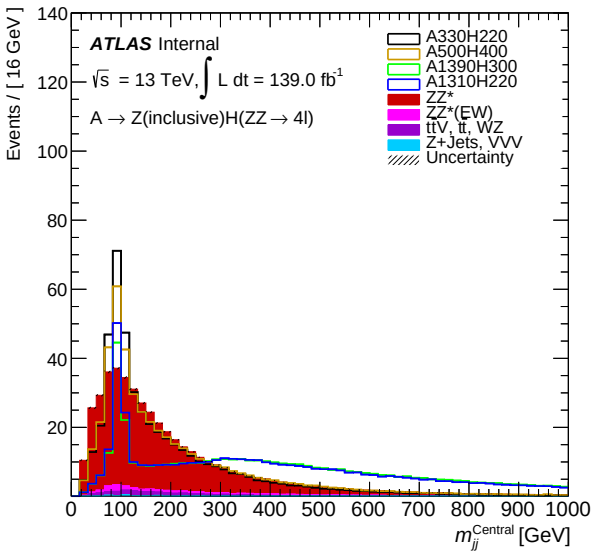

(b)

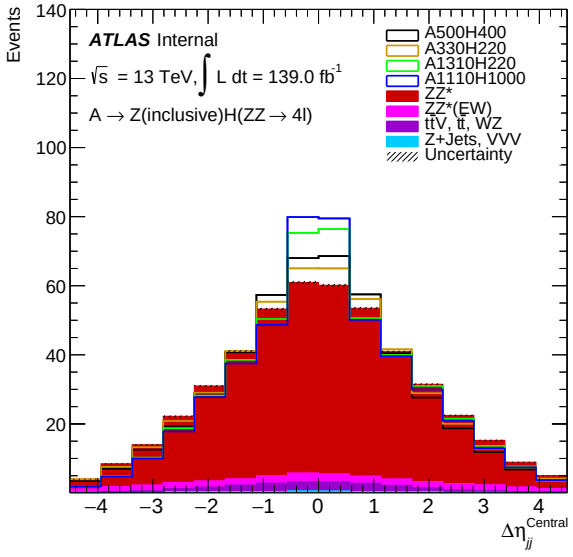

(c)

Figure 8: Distribution for the $A \rightarrow Z(\text{inclusive})H(ZZ \rightarrow 4\ell)$ signal comparing to the different background components of the (a) Dijet transverse momentum, (b) Dijet invariant mass and (c) Dijet $\Delta\eta$. Each signal is normalised to the total number of background.

5 Background estimation

The main background component in all categories comes from the leptonic decay of the Z boson, and it is estimated to be about 98% of the total expected background events. The quark-antiquark annihilation, $q\bar{q} \to ZZ^*$, is 85% and approximately 12% from the gluon-initiated, $gg \to ZZ^*$, processes. And only 1% accounting from EW vector-boson scattering, $q\bar{q} \to ZZ(\text{EW})$.

All other background processes such as WZ, Z+jets, VVV and $t\bar{t}$ are estimated to be nearly 2% from the whole background events.

5.1 $q\bar{q} \to ZZ^*$ and $gg \to ZZ^*$

The $q\bar{q} \to ZZ^*$ and $gg \to ZZ^*$ processes are estimated using MC simulation. Their shapes are modelled by an analytical function on a template denoted by ZZ^*, as shown in Section 6.

5.2 VVV

Because VVV has a different shape from the rest of the backgrounds, it kept on a separate template and fitted with analytical function, see Section 6.

5.3 Other background processes

Other backgrounds which have the same shape are combined together and fitted with analytical function. The template contains WZ, $q\bar{q} \to ZZ(\text{EW})$ and $t\bar{t}$ backgrounds. Z+jets has only one event with large statistical uncertainty at $m_{4\ell}$ between 200-400 GeV so it is removed from the fit, see details in Section 6.

5.4 Control regions

A control region is defined by applying the selection for the High-$E_{\text{T}}^{\text{miss}}$ and $N_{\text{jets}}^{\text{Central}} = 0$ category, as specified in Section 4, to check the compatibility of the data to the prediction. In addition $m_{4\ell}$ region orthogonal to the signal region described by $80 < m_{4\ell} < 110$ GeV and $140 < m_{4\ell} < 170$ GeVis applied.

Table 4: The expected and observed events in a control region of $80 < m_{4\ell} < 110$ GeV and $140 < m_{4\ell} < 170$ GeVfor the High-$E_{\text{T}}^{\text{miss}}$ and $N_{\text{jets}}^{\text{Central}} = 0$ category at 139.0 fb^{-1}.

	ZZ^*	VVV	$q\bar{q} \to ZZ(EW), t\bar{t}V, t\bar{t}$, WZ, Z+jets	Expected	Observed
$2\mu 2e$	10.62±0.32	0.21±0.01	1.12±0.13	11.95±0.34	13.00±3.61
$4e$	5.06±0.21	0.08±0.01	0.41±0.08	5.57±0.23	8.00±2.83
4μ	11.17±0.32	0.15±0.01	0.44±0.09	11.78±0.33	13.00±3.61
4ℓ	26.85±0.50	0.45±0.02	1.99±0.18	29.29±0.53	34.00±5.83

Table 4 shows the number of events after the application of the control region for data and background processes. Figure 10 the shows number of jets, b-tagged jets and $E_{\text{T}}^{\text{miss}}$ significance. The number of jets and

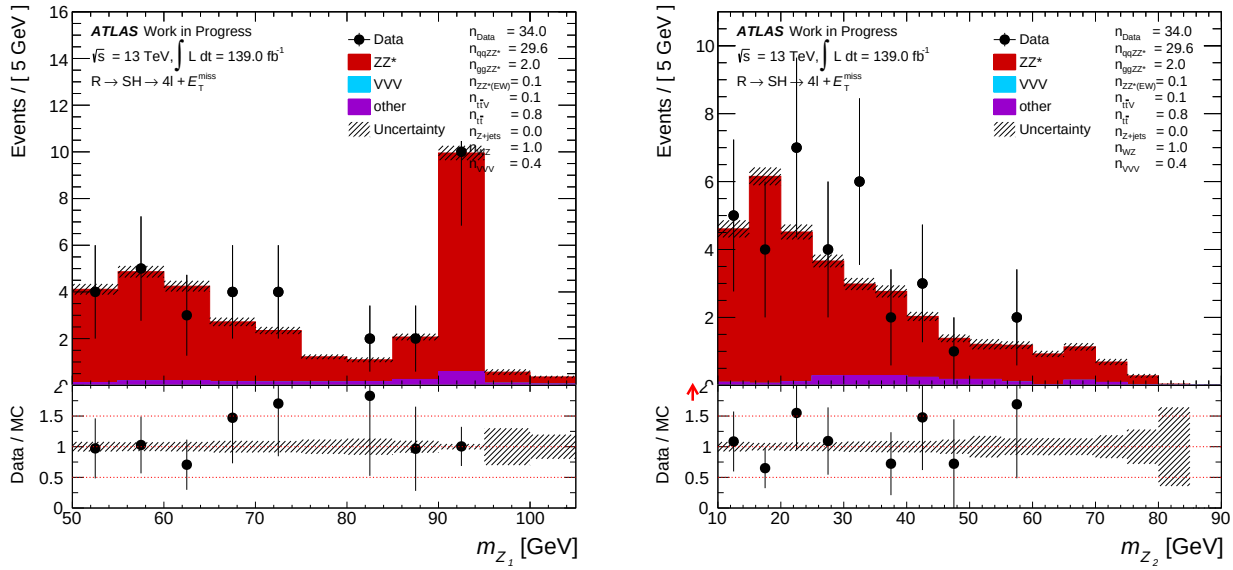

(a) (b)

Figure 9: Kinematic distributions of (a) the m_{Z_1}, (b) and m_{Z_2}. The date at integrated luminosity of 139.0 fb^{-1}are compared to prediction from simulation on the control region. The control region is defined by applying the selection for the High-$E_{\mathrm{T}}^{\mathrm{miss}}$ and $N_{\mathrm{jets}}^{\mathrm{Central}} = 0$ category in the 4-leptons invariant mass region of $80 < m_{4\ell} < 110$ GeV and $140 < m_{4\ell} < 170$ GeV.

b-jets are shown without requirement on the number of jets and b-tagged jets. The four leptons kinematic distributions are shown in Figure 11 for the invariant mass, transverse momentum, pseudorapidity and rapidity of the four leptons final states. Figure 12 shows the momentum of individual leptons, $p_{\mathrm{T}}^{\ell_1}$, $p_{\mathrm{T}}^{\ell_2}$, $p_{\mathrm{T}}^{\ell_3}$ and $p_{\mathrm{T}}^{\ell_4}$. Distributions of the invariant mass of the dilepton system for the first and second lepton pairs m_{Z_1}, m_{Z_2}, respectively, are shown in Figure 9.

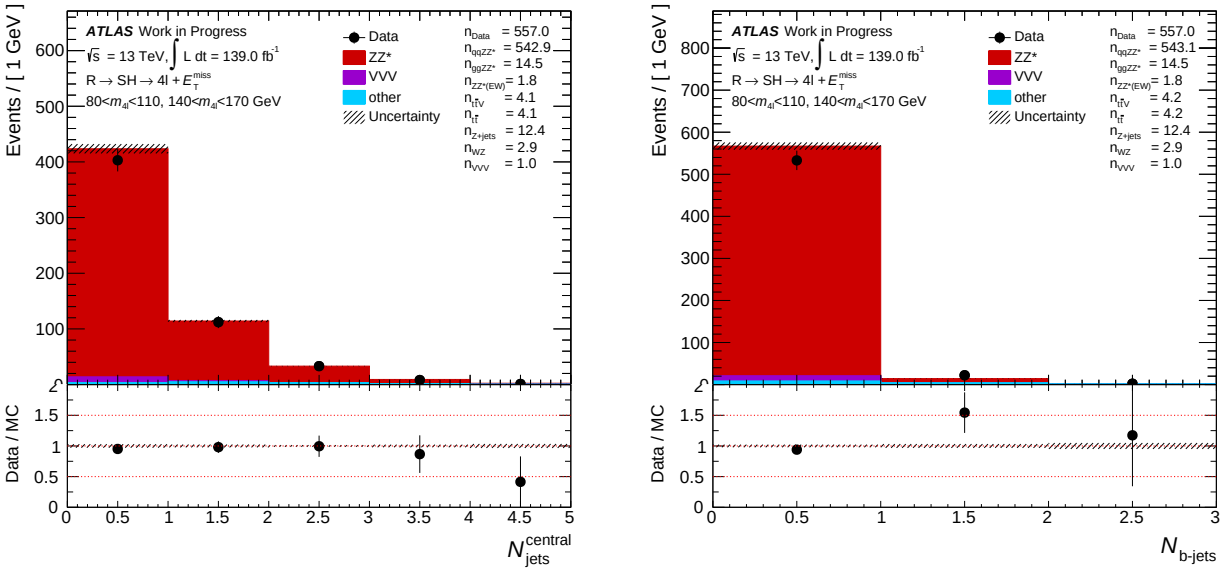

Figure 10: Kinematic distributions of (a) number of central jets, (b) number of b-tagged jets and (c) $E_{\mathrm{T}}^{\mathrm{miss}}$ significance. The date at integrated luminosity of 139.0 fb^{-1} are compared to prediction from simulation on the control region. The control region is defined by applying the selection for the High-$E_{\mathrm{T}}^{\mathrm{miss}}$ and $N_{\mathrm{jets}}^{\mathrm{Central}} = 0$ category in the 4-leptons invariant mass region of $80 < m_{4\ell} < 110$ GeV and $140 < m_{4\ell} < 170$ GeV. The number of jets and b-tagged jets are drawn without applying cut on them.

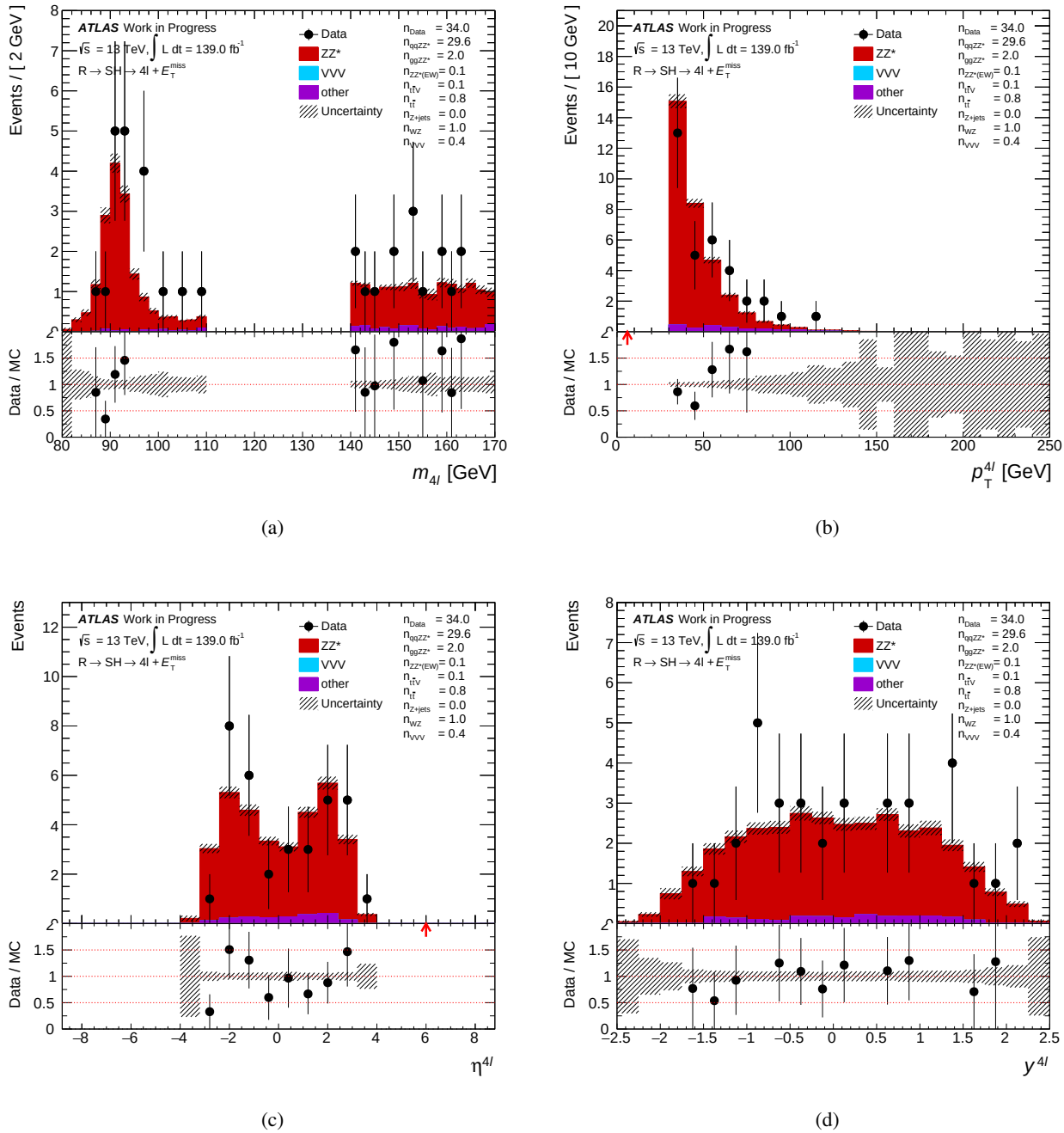

Figure 11: Kinematic distributions of (a) the $m_{4\ell}$, (b) $p_T^{4\ell}$, (c) $\eta^{4\ell}$, and (d) $y^{4\ell}$. The date at integrated luminosity of 139.0 fb^{-1} are compared to prediction from simulation on the control region. The control region is defined by applying the selection for the High-$E_{\mathrm{T}}^{\mathrm{miss}}$ and $N_{\mathrm{jets}}^{\mathrm{Central}} = 0$ category in the 4-leptons invariant mass region of $80 < m_{4\ell} < 110$ GeV and $140 < m_{4\ell} < 170$ GeV.

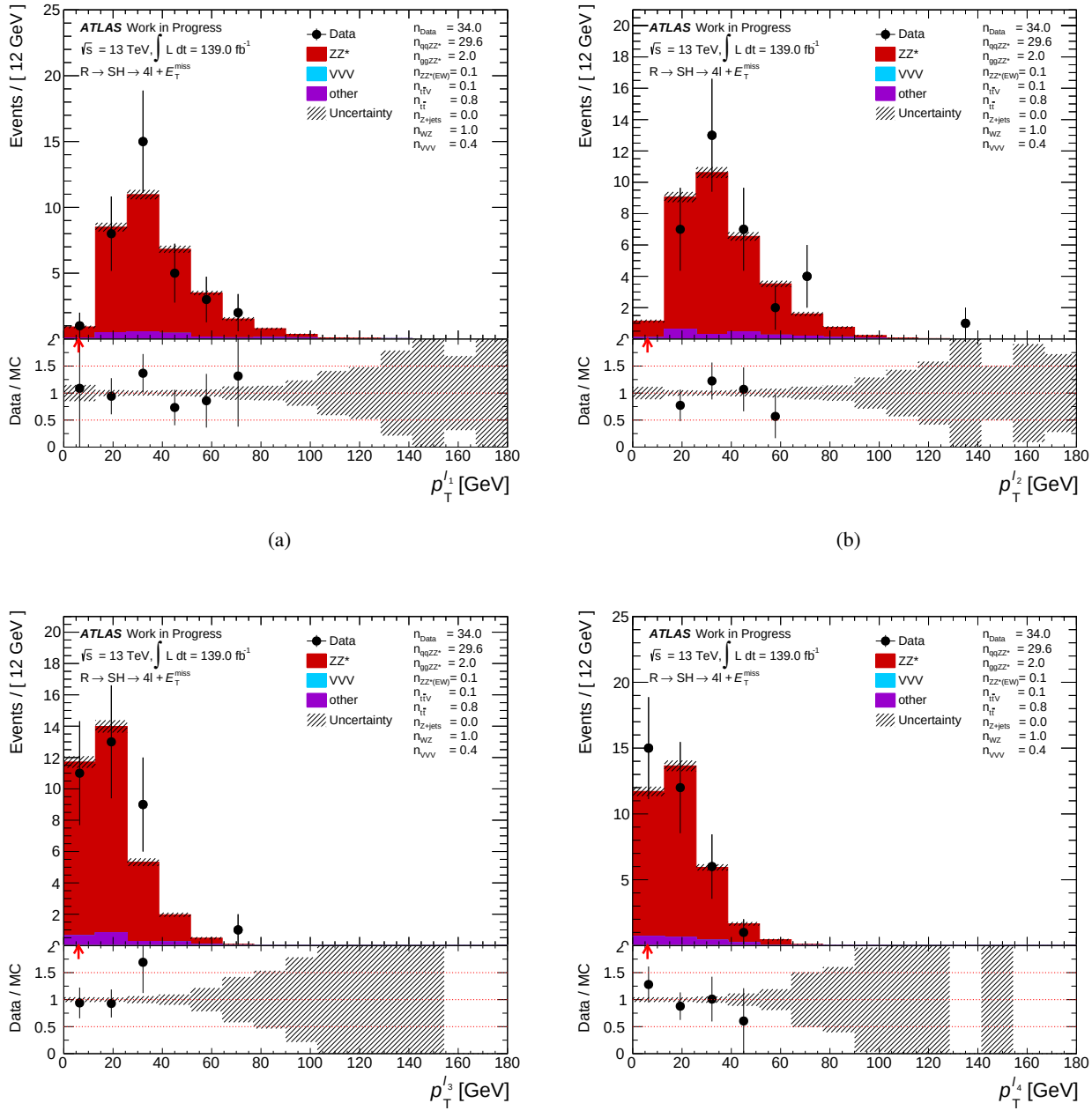

(a) (b)

(c) (d)

Figure 12: Kinematic distributions of (a) the $p_{\mathrm{T}}^{\ell_1}$, (b) $p_{\mathrm{T}}^{\ell_2}$, (c) $p_{\mathrm{T}}^{\ell_3}$, and (d) $p_{\mathrm{T}}^{\ell_4}$. The date at integrated luminosity of 139.0 fb^{-1}are compared to prediction from simulation on the control region. The control region is defined by applying the selection for the High-$E_{\mathrm{T}}^{\mathrm{miss}}$ and $N_{\mathrm{jets}}^{\mathrm{Central}} = 0$ category in the 4-leptons invariant mass region of $80 < m_{4\ell} < 110$ GeV and $140 < m_{4\ell} < 170$ GeV.

6 Signal and background modelling

Monte Carlo simulation is used to parametrise the constructed four leptons invariant mass distribution of both backgrounds and signals shapes. This section explains the signal and background parametrisation.

6.1 Signal parametrisation

The narrow-width signal models of $R \rightarrow SH \rightarrow 4\ell + E_{\mathrm{T}}^{\mathrm{miss}}$ and $A \rightarrow Z(\mathrm{inclusive})H(ZZ \rightarrow 4\ell)$ signals are modelled using a Crystal ball ($\mathcal{CB}$) plus Gaussian ($\mathcal{G}$) functions [17, 18]. The sum of these functions is described as:

$$P_{\mathrm{signal}}(m_{4\ell}) = f_{\mathcal{CB}} \times \mathcal{CB}(m_{4\ell}; \mu, \sigma_{\mathcal{CB}}, \alpha_{\mathcal{CB}}, n_{\mathcal{CB}}) + (1 - f_{\mathcal{CB}}) \times \mathcal{G}(m_{4\ell}; \mu, \sigma_{\mathcal{G}}).$$

Both $\mathcal{CB}$ and $\mathcal{G}$ functions peak at a mean value of $m_{4\ell}(\mu) = m_H$ which is the reconstructed 4-lepton invariant mass of (m_R, m_H) and (m_A, m_H) signal mass points. The resolution of the $m_{4\ell}$ distribution is contorted by $\sigma_{\mathcal{CB}}$ and $\sigma_{\mathcal{G}}$ parameters. The power-law low-end tail position of the non-Gaussian distribution is adjusted using the $\alpha_{\mathcal{CB}}$ parameter, while its slope is handled by the $n_{\mathcal{CB}}$ parameter. The relative normalisation between the Gaussian and Crystal ball functions is taking care of by $f_{\mathcal{CB}}$ parameter. The $P_{\mathrm{signal}}(m_{4\ell})$ function is fitted to simulated signal samples to determine the values of the function's parameters.

The MC samples used are from mc16a, mc16d and mc16e campaigns which add-up to 139.0 fb^{-1}luminosity of Run-II dataset. For simplicity and to avoid lower statistics, the $\mathcal{CB} + \mathcal{G}$ PDF fit is performed to the inclusive lepton channel only to extract the parameter on equation 6.1. Figures 13, 14, 15 and 16 show the $\mathcal{CB} + \mathcal{G}$ PDF fit to $R \rightarrow SH \rightarrow 4\ell + E_{\mathrm{T}}^{\mathrm{miss}}$ of 65 signal mass points. The values of χ^2/ndof illustrates the goodness of the PDF fit. Table 5 shows χ^2/ndof values result from fitting $\mathcal{CB} + \mathcal{G}$ PDF to $R \rightarrow SH \rightarrow 4\ell + E_{\mathrm{T}}^{\mathrm{miss}}$ model for the High-$E_{\mathrm{T}}^{\mathrm{miss}}$ and $N_{\mathrm{jets}}^{\mathrm{Central}} = 0$ category. The other categories are shown in appendix A.

Table 5: Summary of χ^2/ndof values from fitting $\mathcal{CB} + \mathcal{G}$ PDF of equation 6.1 to different mass points of the $R \rightarrow SH \rightarrow 4\ell + E_{\mathrm{T}}^{\mathrm{miss}}$ model for the High-$E_{\mathrm{T}}^{\mathrm{miss}}$ and $N_{\mathrm{jets}}^{\mathrm{Central}} = 0$ category. The χ^2/ndof are shown for Figures 13, 14, 15 and 16.

Mass point = (m_X, m_H) [GeV]	χ^2/ndof	Mass point = (m_X, m_H) [GeV]	χ^2/ndof	Mass point = (m_X, m_H) [GeV]	χ^2/ndof	Mass point = (m_X, m_H) [GeV]	χ^2/ndof
390, 220	0.98	470, 300	1.21	600, 400	1.34	760, 400	1.46
450, 220	1.58	570, 400	1.08	700, 500	1.86	860, 500	1.40
800, 220	1.29	770, 600	1.14	800, 600	1.69	960, 600	1.13
1500, 220	1.90	970, 800	1.43	1000, 800	1.75	1160, 800	1.78
450, 250	1.35	430, 250	1.28	1200, 1000	2.00	1360, 1000	2.18
1500, 250	1.73	480, 300	0.80	460, 250	1.85	910, 250	1.43
800, 300	1.48	580, 400	0.99	510, 300	1.09	960, 300	1.95
800, 500	1.57	680, 500	1.12	610, 400	2.04	1060, 400	1.32
1500, 1000	1.75	780, 600	1.75	710, 500	1.48	1160, 500	1.73
410, 220	1.33	980, 800	1.77	810, 600	1.31	1260, 600	0.98
430, 220	1.37	1180, 1000	1.82	1010, 800	1.42	1460, 800	1.88
580, 220	1.71	440, 250	1.10	1210, 1000	1.86	1660, 1000	1.56
880, 220	1.15	490, 300	1.21	510, 250	1.10	1410, 250	1.54
1380, 220	1.40	590, 400	2.26	560, 300	1.49	1460, 300	1.60
670, 500	1.06	690, 500	1.29	660, 400	1.56	1560, 400	2.64
610, 250	1.51	790, 600	1.76	760, 500	1.85	1660, 500	2.00
660, 300	1.58	990, 800	1.98	860, 600	1.33	1760, 600	1.78
1170, 1000	0.85	1190, 1000	1.44	1060, 800	1.58	1960, 800	1.98
-	-	500, 300	1.72	1260, 1000	1.72	2160, 1000	1.88

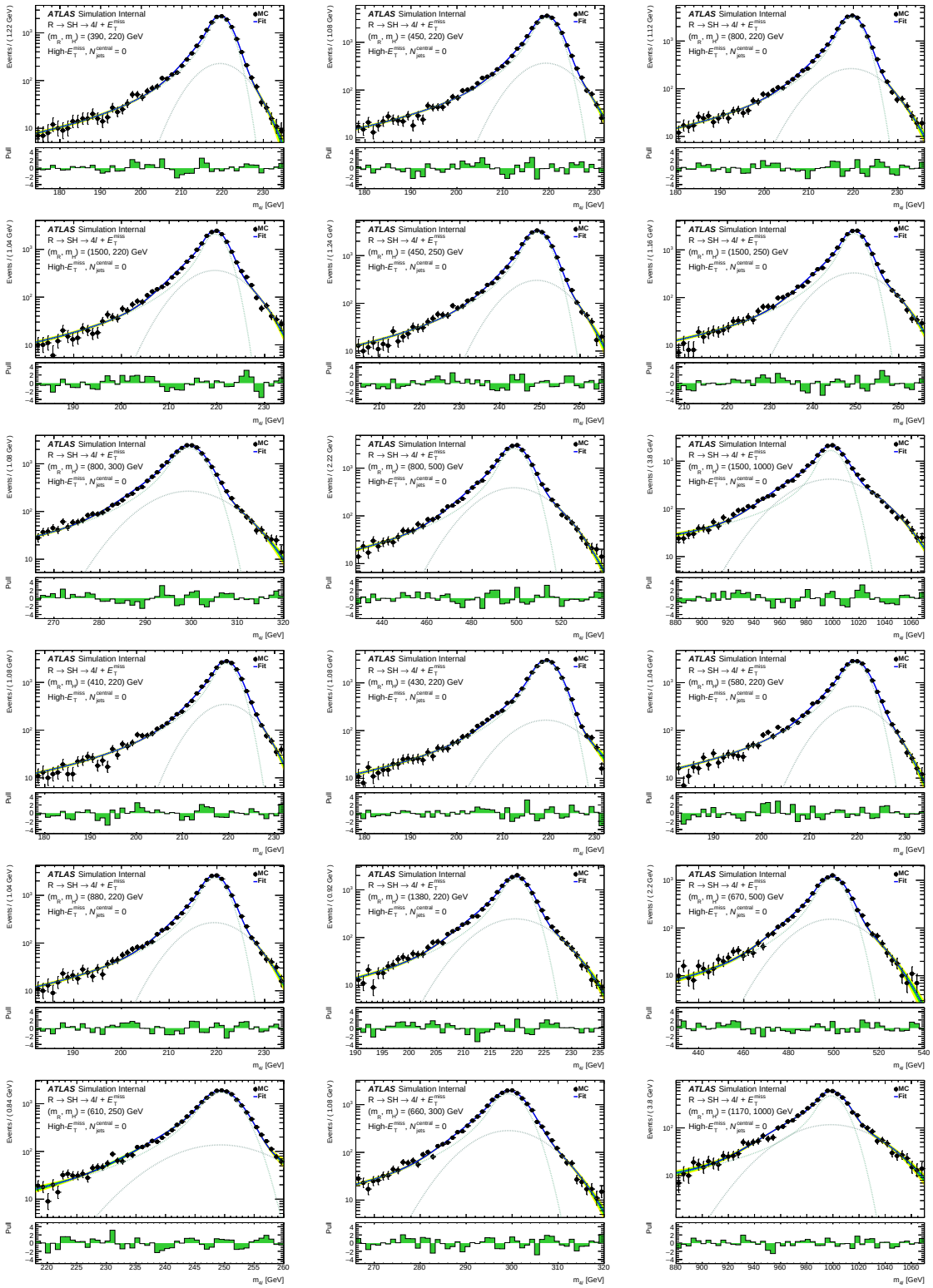

Figure 13: Distributions of the four-lepton invariant mass for fitting the $\mathcal{CB}+\mathcal{G}$ PDF of equation 6.1 to (390,220), (450,220), (800,220), (1500,220), (450,250), (1500,250), (800,300), (800,500), (1500,1000), (410,220), (430,220), (580,220), (880,220), (1380,220), (670,500), (610,250), (660,300) and (1170,1000) GeV signal mass points for the $R \to SH \to 4\ell + E_{\mathrm{T}}^{\mathrm{miss}}$ model. MC simulation of statistics equivalent to integrated luminosity of 139.0 fb^{-1}is used for the High-$E_{\mathrm{T}}^{\mathrm{miss}}$ and $N_{\mathrm{jets}}^{\mathrm{Central}} = 0$ category. The ratio plot in each figure shows the pull distribution.

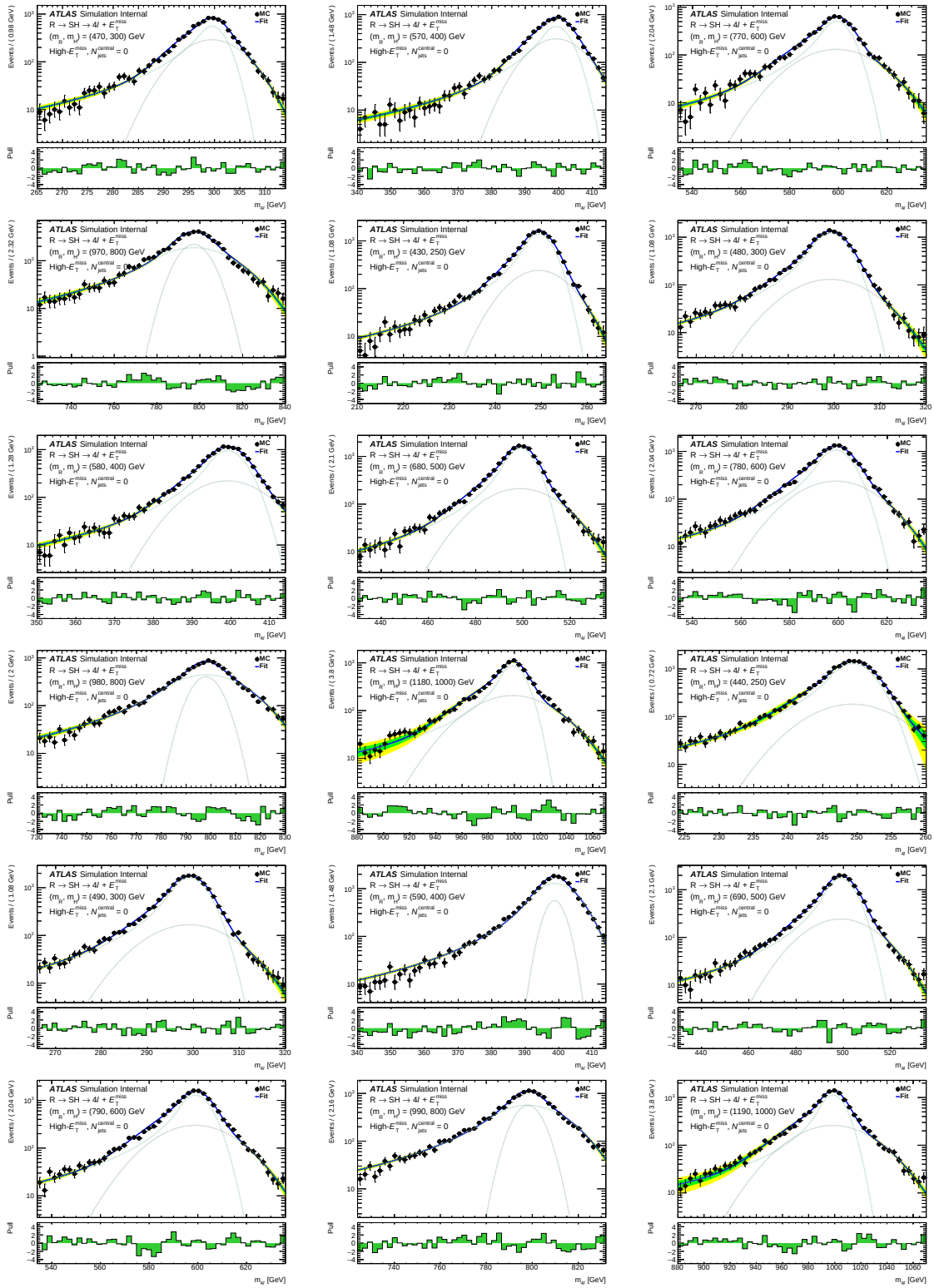

Figure 14: Distributions of the four-lepton invariant mass for fitting the $\mathcal{CB}+\mathcal{G}$ PDF of equation 6.1 to (470,300), (570,400), (770,600), (970,800), (430,250), (480,300), (580,400), (680,500), (780,600), (980,800), (1180,1000), (440,250), (490,300), (590,400), (690,500), (790,600), (990,800) and (1190,1000) GeV signal mass points for the $R \rightarrow SH \rightarrow 4\ell + E_{\mathrm{T}}^{\mathrm{miss}}$ model. MC simulation of statistics equivalent to integrated luminosity of 139.0 fb^{-1}is used for the High-$E_{\mathrm{T}}^{\mathrm{miss}}$ and $N_{\mathrm{jets}}^{\mathrm{Central}} = 0$ category. The ratio plot in each figure shows the pull distribution.

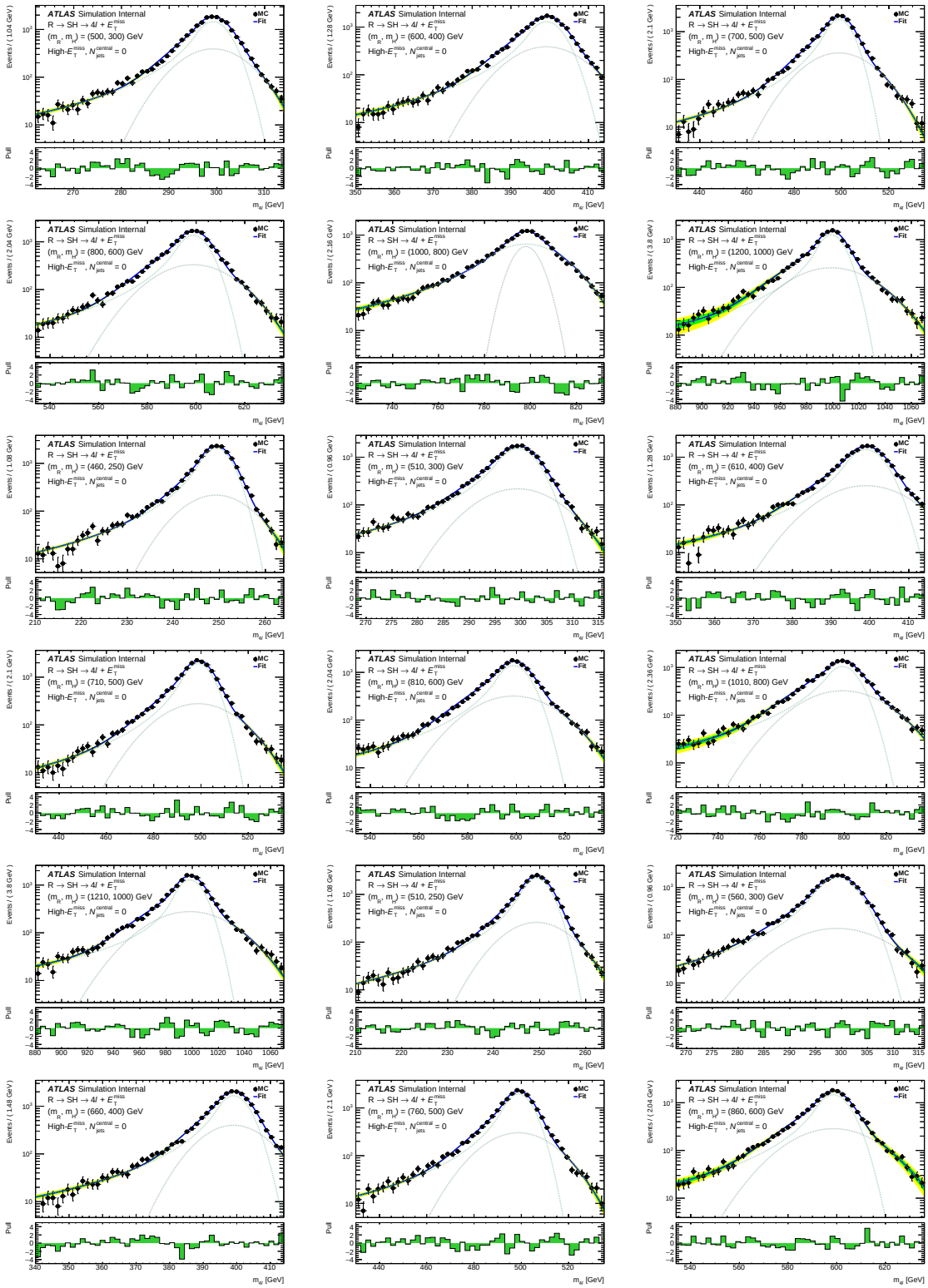

Figure 15: Distributions of the four-lepton invariant mass for fitting the $\mathcal{CB}+\mathcal{G}$ PDF of equation 6.1 to (500,300), (600,400), (800,600), (1000,800), (1000,800), (1200,1000), (460,250), (510,300), (610,400), (710,500), (810,600), (1010,800), (1210,1000), (510,250), (560,300), (660,400), (760,500) and (860,600) GeV signal mass points for the $R \rightarrow SH \rightarrow 4\ell + E_{\mathrm{T}}^{\mathrm{miss}}$ model. MC simulation of statistics equivalent to integrated luminosity of 139.0 fb^{-1}is used for the High-$E_{\mathrm{T}}^{\mathrm{miss}}$ and $N_{\mathrm{jets}}^{\mathrm{Central}} = 0$ category. The ratio plot in each figure shows the pull distribution.

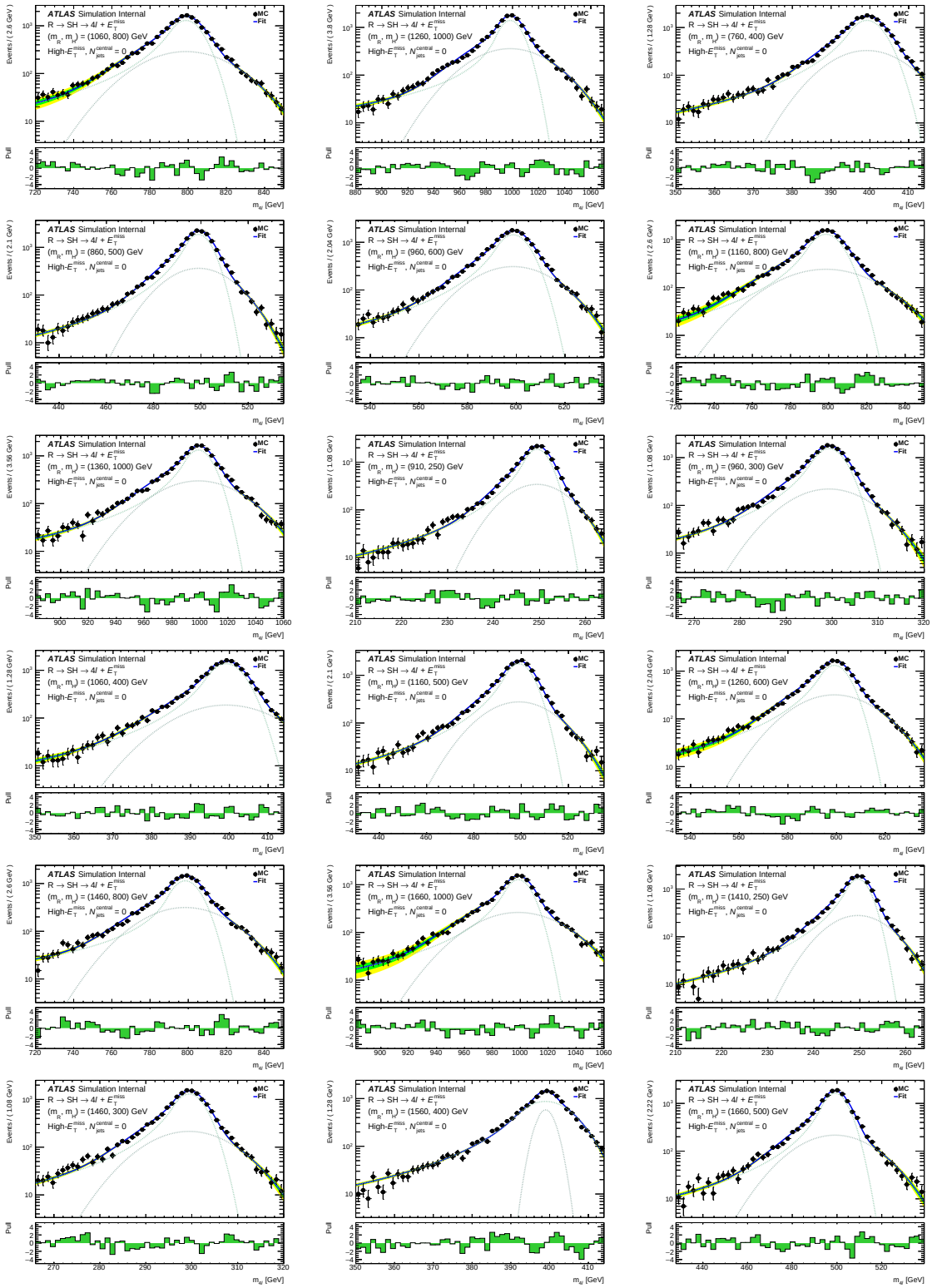

Figure 16: Distributions of the four-lepton invariant mass for fitting the $\mathcal{CB} + \mathcal{G}$ PDF of equation 6.1 to (1060,800), (1260,1000), (760,400), (860,500), (960,600), (1160,800), (1360,1000), (910,250), (960,300), (1060,400), (1160,500), (1260,600), (1460,800), (1660,1000), (1410,250), (1460,300), (1560,400) and (1660,500) GeV signal mass points for the $R \rightarrow SH \rightarrow 4\ell + E_{\mathrm{T}}^{\mathrm{miss}}$ model. MC simulation of statistics equivalent to integrated luminosity of 139.0 fb^{-1}is used for the High-$E_{\mathrm{T}}^{\mathrm{miss}}$ and $N_{\mathrm{jets}}^{\mathrm{Central}} = 0$ category. The ratio plot in each figure shows the pull distribution.

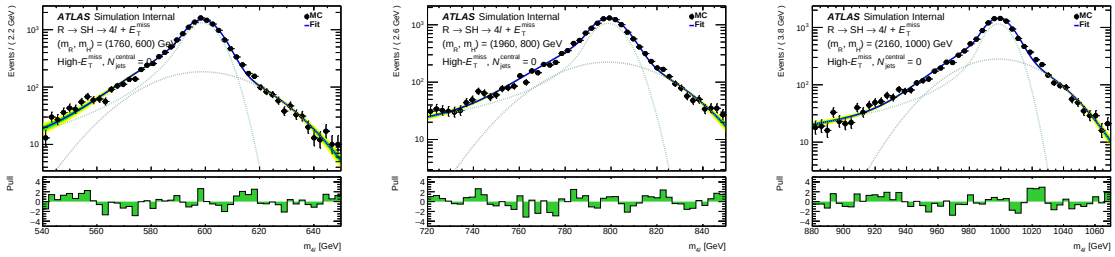

Figure 17: Distributions of the four-lepton invariant mass for fitting the $\mathcal{CB} + \mathcal{G}$ PDF of equation 6.1 to (1760,600), (1960,800) and (2160,1000) GeV signal mass points for the $R \rightarrow SH \rightarrow 4\ell + E_{\mathrm{T}}^{\mathrm{miss}}$ model. MC simulation of statistics equivalent to integrated luminosity of 139.0 fb^{-1}is used for the High-$E_{\mathrm{T}}^{\mathrm{miss}}$ and $N_{\mathrm{jets}}^{\mathrm{Central}} = 0$ category. The ratio plot in each figure shows the pull distribution.

6.2 Background parametrisation

$$f^{ggZZ/qqZZ}(m_{4\ell}) = (f_1(m_{4\ell}) + f_2(m_{4\ell})) \times H(m_0 - m_{4\ell}) \times C_0 + f_3^{ggZZ/qqZZ}(m_{4\ell}) \times H(m_{4\ell} - m_0),$$

where:

$$\begin{aligned}
f_1(m_{4\ell}) &= \exp(a_1 + a_2 \cdot m_{4\ell} + a_3 \cdot m_{4\ell}^2), \\
f_2(m_{4\ell}) &= \left\{\frac{1}{2} + \frac{1}{2}\,\mathrm{erf}\left(\frac{m_{4\ell} - b_1}{b_2}\right)\right\} \times \frac{1}{1 + \exp\left(\frac{m_{4\ell} - b_1}{b_3}\right)}, \\
f_3^{qqZZ/ggZZ}(m_{4\ell}) &= \exp\left(c_1 + c_2 \cdot m_{4\ell} + c_3 \cdot m_{4\ell}^2 + c_4 \cdot m_{4\ell}^3 + c_5 \cdot m_{4\ell}^4 + c_6 \cdot m_{4\ell}^5\right), \\
C_0 &= \frac{f_3(m_0)}{f_1(m_0) + f_2(m_0)}.
\end{aligned}$$

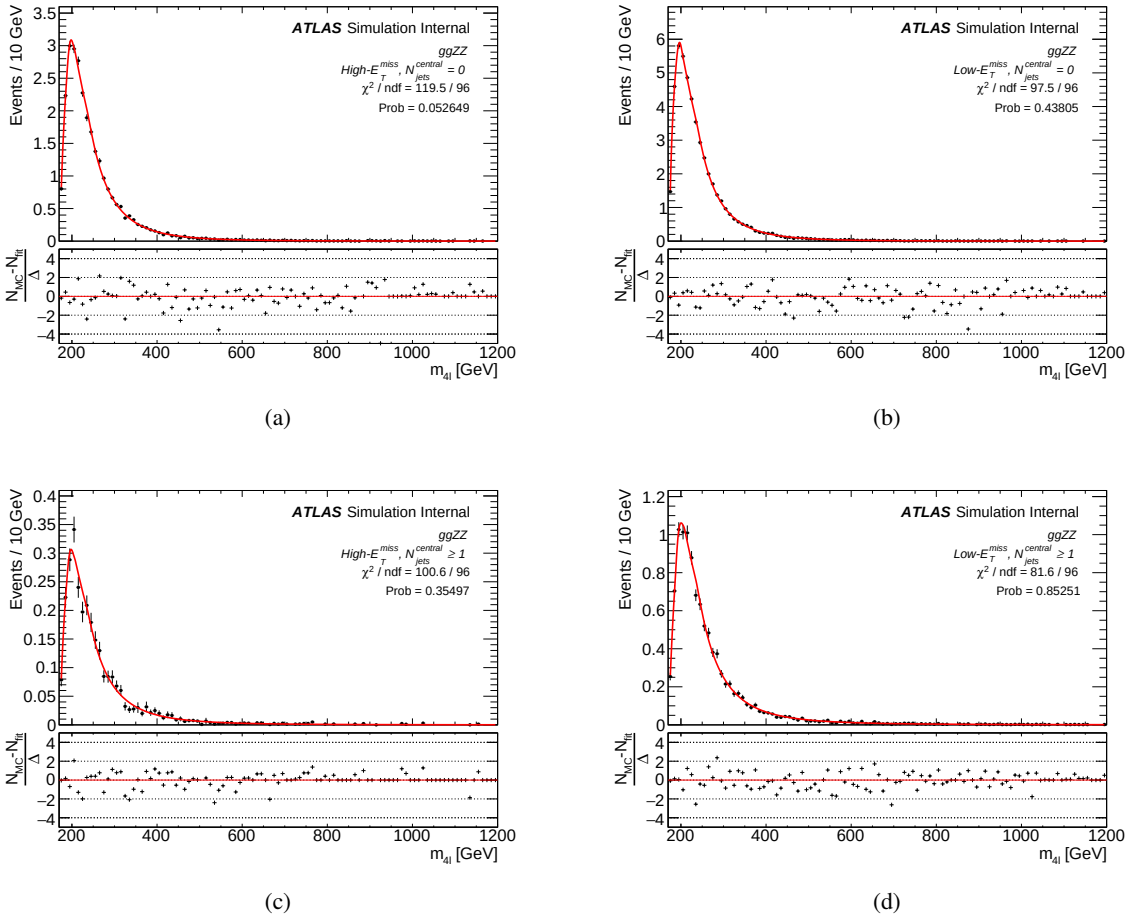

(a) (b)

(c) (d)

Figure 18: Four-lepton invariant mass distributions for the analytical function fit to ZZ^* background template of the (a) High-$E_{\mathrm{T}}^{\mathrm{miss}}$ and $N_{\mathrm{jets}}^{\mathrm{Central}} = 0$, (b) Low-$E_{\mathrm{T}}^{\mathrm{miss}}$ and $N_{\mathrm{jets}}^{\mathrm{Central}} = 0$, (c) High-$E_{\mathrm{T}}^{\mathrm{miss}}$ and $N_{\mathrm{jets}}^{\mathrm{Central}} \geq 1$, (d) Low-$E_{\mathrm{T}}^{\mathrm{miss}}$ and $N_{\mathrm{jets}}^{\mathrm{Central}} \geq 1$ categories.

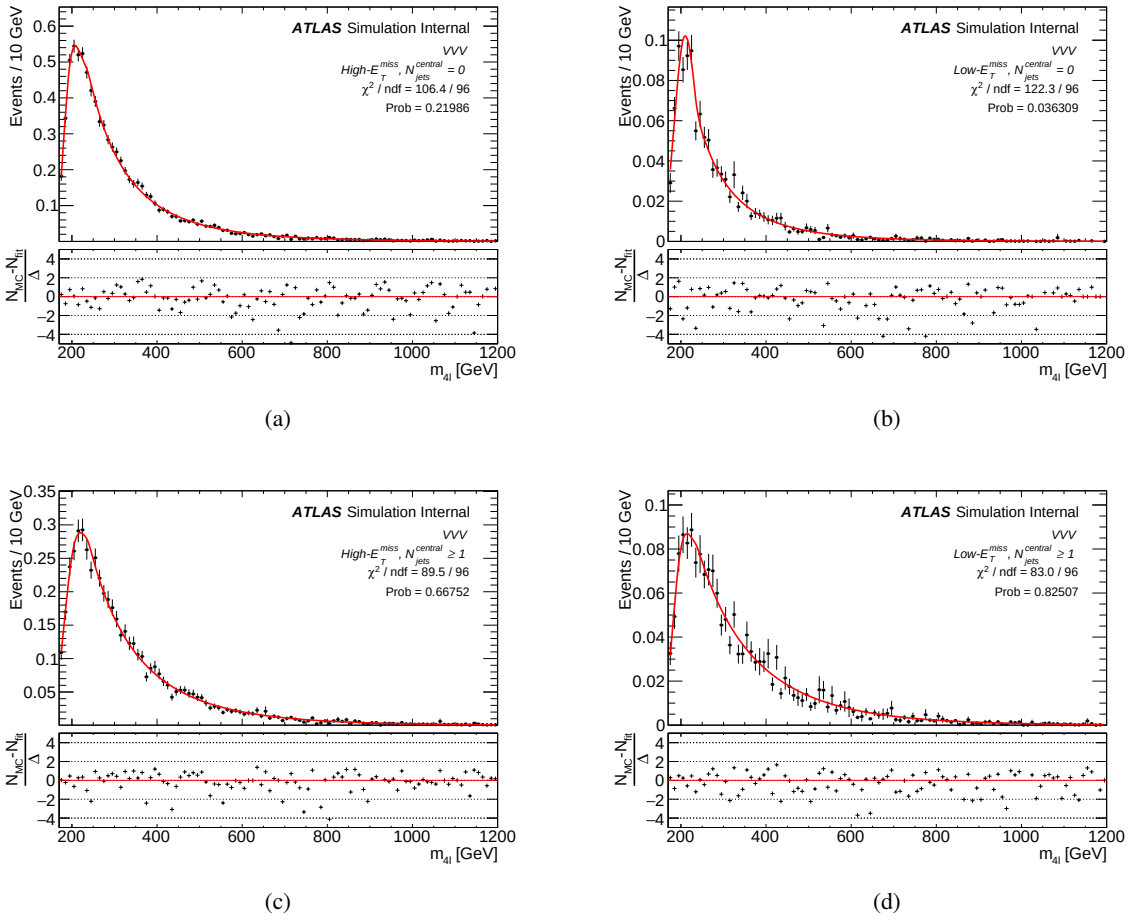

Figure 19: Four-lepton invariant mass distributions for the analytical function fit to *VVV* background of the (a) High-$E_{\mathrm{T}}^{\mathrm{miss}}$ and $N_{\mathrm{jets}}^{\mathrm{Central}} = 0$, (b) Low-$E_{\mathrm{T}}^{\mathrm{miss}}$ and $N_{\mathrm{jets}}^{\mathrm{Central}} = 0$, (c) High-$E_{\mathrm{T}}^{\mathrm{miss}}$ and $N_{\mathrm{jets}}^{\mathrm{Central}} \geq 1$, (d) Low-$E_{\mathrm{T}}^{\mathrm{miss}}$ and $N_{\mathrm{jets}}^{\mathrm{Central}} \geq 1$ categories.

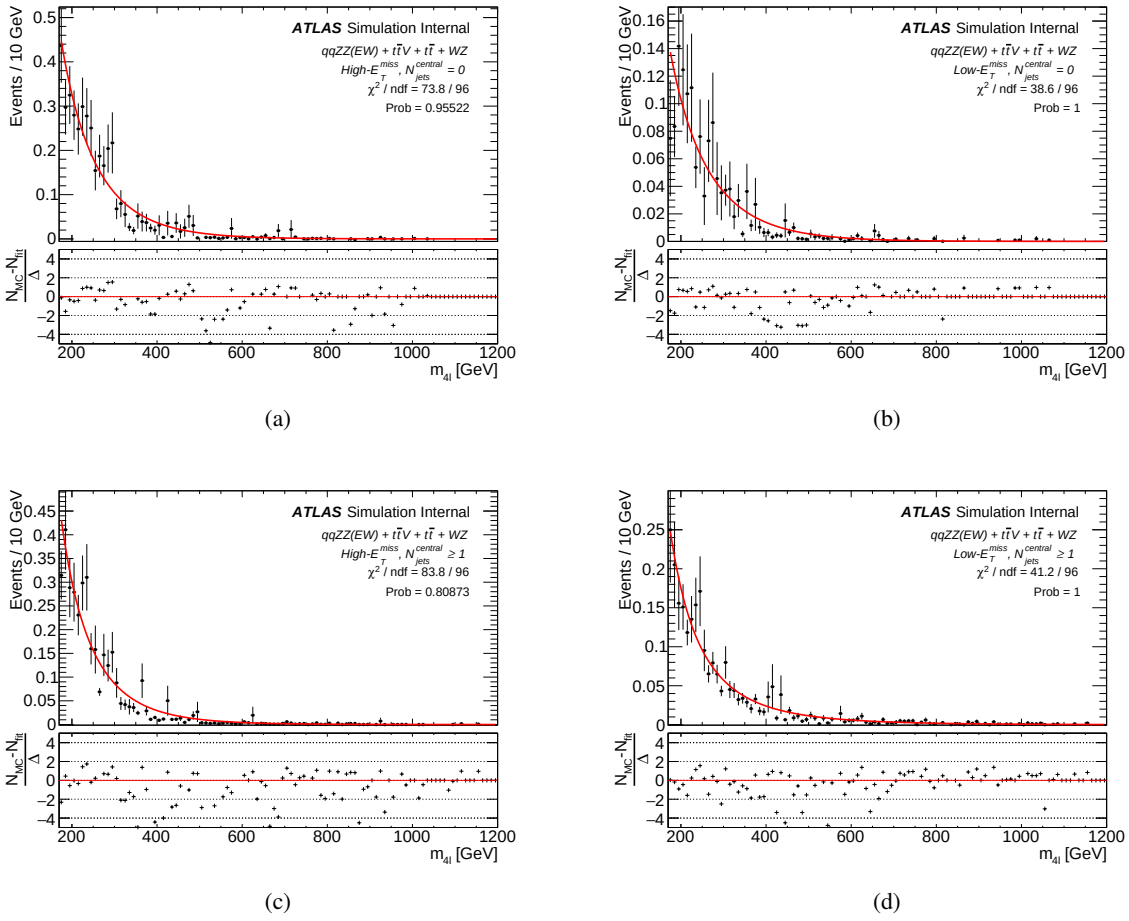

Figure 20: Four-lepton invariant mass distributions for the analytical function fit to $q\bar{q} \to ZZ^*$(EW), WZ, $t\bar{t}$ and $t\bar{t}V$ background template of the (a) High-$E_{\mathrm{T}}^{\mathrm{miss}}$ and $N_{\mathrm{jets}}^{\mathrm{Central}} = 0$, (b) Low-$E_{\mathrm{T}}^{\mathrm{miss}}$ and $N_{\mathrm{jets}}^{\mathrm{Central}} = 0$, (c) High-$E_{\mathrm{T}}^{\mathrm{miss}}$ and $N_{\mathrm{jets}}^{\mathrm{Central}} \geq 1$, (d) Low-$E_{\mathrm{T}}^{\mathrm{miss}}$ and $N_{\mathrm{jets}}^{\mathrm{Central}} \geq 1$ categories.

7 Systematic uncertainties

7.1 Experimental systematic uncertainties

7.2 Theoretical systematic uncertainties

Normalisation	Shape
Electrons	
	EG_RESOLUTION_ALL
EL_EFF_ID_CorrUncertaintyNP[0-15]	EG_SCALE_ALLCORR
EL_EFF_ID_SIMPLIFIED_UncorrUncertaintyNP[0-17]	EG_SCALE_E4SCINTILLATOR
EL_EFF_Iso_TOTAL_1NPCOR_PLUS_UNCOR	EG_SCALE_LARCALIB_EXTRA2015PRE
EL_EFF_Reco_TOTAL_1NPCOR_PLUS_UNCOR	EG_SCALE_LARTEMPERATURE_EXTRA2015PRE
	EG_SCALE_LARTEMPERATURE_EXTRA2016PRE
Muons	
MUON_EFF_ISO_STAT	
MUON_EFF_ISO_SYS	
MUON_EFF_RECO_STAT	MUON_ID
MUON_EFF_RECO_STAT_LOWPT	MUON_MS
MUON_EFF_RECO_SYS	MUON_SAGITTA_RESBIAS
MUON_EFF_RECO_SYS_LOWPT	MUON_SAGITTA_RHO
MUON_EFF_TTVA_STAT	MUON_SCALE
MUON_EFF_TTVA_SYS	
Jets	
	JET_BJES_Response
	JET_EffectiveNP_[1-7]
	JET_EffectiveNP_8restTerm
	JET_EtaIntercalibration_Modelling
	JET_EtaIntercalibration_NonClosure_highE
	JET_EtaIntercalibration_NonClosure_negEta
	JET_EtaIntercalibration_NonClosure_posEta
	JET_EtaIntercalibration_TotalStat
	JET_Flavor_Composition
	JET_Flavor_Response
	JET_JER_DataVsMC
	JET_JER_EffectiveNP_[1-6]
	JET_JER_EffectiveNP_7restTerm
	JET_Pileup_OffsetMu
	JET_Pileup_OffsetNPV
	JET_Pileup_PtTerm
	JET_Pileup_RhoTopology
	JET_PunchThrough_MC16
	JET_SingleParticle_HighPt
Missing transverse energy	
	MET_SoftTrk_ResoPara
	MET_SoftTrk_ResoPerp
	MET_SoftTrk_Scale
Other	
HOEW_QCD_syst	
HOEW_syst	
HOQCD_scale_syst	
PRW_DATASF	

8 Results and interpretations

8.1 Statistical procedures

8.2 Results for the $R \to SH \to 4\ell + E_{\mathrm{T}}^{\mathrm{miss}}$ model

8.3 Results for the $A \to Z(\text{inclusive})H(ZZ \to 4\ell)$ model

9 Conclusion

References

[1] ATLAS Collaboration, *Observation of a new particle in the search for the Standard Model Higgs boson with the ATLAS detector at the LHC*, Phys. Lett. B **716** (2012) 1, arXiv: 1207.7214 [hep-ex] (cit. on p. 6).

[2] CMS Collaboration, *Observation of a new boson at a mass of 125 GeV with the CMS experiment at the LHC*, Phys. Lett. B **716** (2012) 30, arXiv: 1207.7235 [hep-ex] (cit. on p. 6).

[3] ATLAS Collaboration, *Measurements of the Higgs boson production and decay rates and coupling strengths using pp collision data at $\sqrt{s} = 7$ and 8 TeV in the ATLAS experiment*, Eur. Phys. J. C **76** (2016) 6, arXiv: 1507.04548 [hep-ex] (cit. on p. 6).

[4] ATLAS Collaboration, *Study of the spin and parity of the Higgs boson in diboson decays with the ATLAS detector*, Eur. Phys. J. C **75** (2015) 476, arXiv: 1506.05669 [hep-ex] (cit. on p. 6), Erratum: Eur. Phys. J. C **76** (2016) 152.

[5] CMS Collaboration, *Precise determination of the mass of the Higgs boson and tests of compatibility of its couplings with the standard model predictions using proton collisions at 7 and 8 TeV*, Eur. Phys. J. C **75** (2015) 212, arXiv: 1412.8662 [hep-ex] (cit. on p. 6).

[6] CMS Collaboration, *Constraints on the spin-parity and anomalous HVV couplings of the Higgs boson in proton collisions at 7 and 8 TeV*, Phys. Rev. D **92** (2015) 012004, arXiv: 1411.3441 [hep-ex] (cit. on p. 6).

[7] H. E. Haber and G. L. Kane, *The Search for Supersymmetry: Probing Physics Beyond the Standard Model*, Phys. Rept. **117** (1985) 75 (cit. on p. 6).

[8] N. Arkani-Hamed, S. Dimopoulos and G. R. Dvali, *The Hierarchy problem and new dimensions at a millimeter*, Phys. Lett. B **429** (1998) 263, arXiv: hep-ph/9803315 (cit. on p. 6).

[9] G. F. Giudice, *Naturally Speaking: The Naturalness Criterion and Physics at the LHC*, 2008, arXiv: 0801.2562 [hep-ph] (cit. on p. 6).

[10] G. C. Branco et al., *Theory and phenomenology of two-Higgs-doublet models*, Phys. Rept. **516** (2012) 1, arXiv: 1106.0034 [hep-ph] (cit. on p. 6).

[11] M. Muhlleitner, M. O. P. Sampaio, R. Santos and J. Wittbrodt, *The N2HDM under Theoretical and Experimental Scrutiny*, JHEP **03** (2017) 094, arXiv: 1612.01309 [hep-ph] (cit. on p. 6).

[12] G. Dorsch, S. Huber, K. Mimasu and J. No, *Echoes of the Electroweak Phase Transition: Discovering a second Higgs doublet through $A_0 \to ZH_0$*, Phys. Rev. Lett. **113** (2014) 211802, arXiv: 1405.5537 [hep-ph] (cit. on p. 6).

[13] ATLAS Collaboration, *Operation and performance of the ATLAS semiconductor tracker*, JINST **9** (2014) P08009, arXiv: 1404.7473 [hep-ex] (cit. on p. 7).

[14] ATLAS Collaboration, *Monitoring and data quality assessment of the ATLAS liquid argon calorimeter*, JINST **9** (2014) P07024, arXiv: 1405.3768 [hep-ex] (cit. on p. 7).

[15] ATLAS Collaboration, *Selection of jets produced in 13 TeV proton–proton collisions with the ATLAS detector*, ATLAS-CONF-2015-029, 2015, URL: https://cds.cern.ch/record/2037702 (cit. on p. 7).

[16] ATLAS Collaboration, *Object-based missing transverse momentum significance in the ATLAS Detector*, ATLAS-CONF-2018-038, 2018, URL: https://cds.cern.ch/record/2630948 (cit. on p. 10).

[17] J. Gaiser, *Charmonium Spectroscopy From Radiative Decays of the J/ψ and ψ'*, 1982, URL: https://www.slac.stanford.edu/cgi-wrap/getdoc/slac-r-255.pdf (cit. on p. 21).

[18] M. Oreglia, *A Study of the Reactions $\psi' \to \gamma\gamma\psi$*, 1980, URL: https://www.slac.stanford.edu/cgi-wrap/getdoc/slac-r-236.pdf (cit. on p. 21).

Appendices

A Signal parametrisation

Table 6: Summary of χ^2/ndof values from fitting $\mathcal{CB} + \mathcal{G}$ PDF of equation 6.1 to different mass points of the $R \rightarrow SH \rightarrow 4\ell + E_{\mathrm{T}}^{\mathrm{miss}}$ model for the Low-$E_{\mathrm{T}}^{\mathrm{miss}}$ and $N_{\mathrm{jets}}^{\mathrm{Central}} = 0$ category. The χ^2/ndof are shown for Figures 21, 22, 23 and 24.

Mass point = (m_X, m_H) [GeV]	χ^2/ndof	Mass point = (m_X, m_H) [GeV]	χ^2/ndof	Mass point = (m_X, m_H) [GeV]	χ^2/ndof	Mass point = (m_X, m_H) [GeV]	χ^2/ndof
390, 220	1.23	470, 300	1.42	600, 400	1.33	760, 400	1.44
450, 220	1.63	570, 400	1.69	700, 500	1.88	860, 500	1.47
800, 220	1.30	770, 600	1.35	800, 600	1.59	960, 600	1.14
1500, 220	1.89	970, 800	2.14	1000, 800	1.85	1160, 800	1.78
450, 250	1.40	430, 250	1.49	1200, 1000	2.26	1360, 1000	2.28
1500, 250	1.72	480, 300	0.97	460, 250	1.85	910, 250	1.45
800, 300	1.50	580, 400	1.13	510, 300	1.09	960, 300	1.95
800, 500	1.60	680, 500	1.31	610, 400	2.03	1060, 400	1.30
1500, 1000	1.83	780, 600	1.75	710, 500	1.53	1160, 500	1.76
410, 220	1.57	980, 800	2.26	810, 600	1.37	1260, 600	0.96
430, 220	1.36	1180, 1000	2.05	1010, 800	1.45	1460, 800	1.93
580, 220	1.73	440, 250	1.32	1210, 1000	2.25	1660, 1000	1.53
880, 220	1.15	490, 300	1.05	510, 250	1.15	1410, 250	1.50
1380, 220	1.41	590, 400	2.44	560, 300	1.45	1460, 300	1.59
670, 500	1.18	690, 500	1.44	660, 400	1.59	1560, 400	2.63
610, 250	1.51	790, 600	1.87	760, 500	1.86	1660, 500	1.98
660, 300	1.58	990, 800	2.12	860, 600	1.36	1760, 600	1.79
1170, 1000	1.05	1190, 1000	1.76	1060, 800	1.66	1960, 800	1.99
-	-	500, 300	1.86	1260, 1000	1.82	2160, 1000	1.89

Table 7: Summary of χ^2/ndof values from fitting $\mathcal{CB} + \mathcal{G}$ PDF of equation 6.1 to different mass points of the $R \rightarrow SH \rightarrow 4\ell + E_{\mathrm{T}}^{\mathrm{miss}}$ model for the High-$E_{\mathrm{T}}^{\mathrm{miss}}$ and $N_{\mathrm{jets}}^{\mathrm{Central}} \geq 1$ category. The χ^2/ndof are shown for Figures 26, 27, 28 and 29.

Mass point = (m_X, m_H) [GeV]	χ^2/ndof	Mass point = (m_X, m_H) [GeV]	χ^2/ndof	Mass point = (m_X, m_H) [GeV]	χ^2/ndof	Mass point = (m_X, m_H) [GeV]	χ^2/ndof
390, 220	1.26	470, 300	1.31	600, 400	1.29	760, 400	1.70
450, 220	1.92	570, 400	0.54	700, 500	1.82	860, 500	3.07
800, 220	2.13	770, 600	0.83	800, 600	1.59	960, 600	2.63
1500, 220	2.64	970, 800	1.14	1000, 800	3.01	1160, 800	3.76
450, 250	1.41	430, 250	1.06	1200, 1000	1.62	1360, 1000	8.05
1500, 250	3.23	480, 300	1.79	460, 250	1.15	910, 250	7.68
800, 300	2.09	580, 400	0.76	510, 300	1.84	960, 300	1.67
800, 500	2.65	680, 500	1.60	610, 400	1.14	1060, 400	2.08
1500, 1000	5.79	780, 600	1.29	710, 500	2.10	1160, 500	3.69
410, 220	1.51	980, 800	1.10	810, 600	1.81	1260, 600	8.69
430, 220	1.28	1180, 1000	1.45	1010, 800	1.62	1460, 800	2.50
580, 220	1.40	440, 250	1.01	1210, 1000	1.68	1660, 1000	7.62
880, 220	1.87	490, 300	1.17	510, 250	1.30	1410, 250	2.78
1380, 220	3.27	590, 400	2.13	560, 300	4.74	1460, 300	2.92
670, 500	0.90	690, 500	1.32	660, 400	1.12	1560, 400	4.57
610, 250	2.15	790, 600	1.79	760, 500	1.95	1660, 500	4.47
660, 300	2.73	990, 800	1.84	860, 600	2.83	1760, 600	4.28
1170, 1000	0.91	1190, 1000	1.62	1060, 800	3.02	1960, 800	2.50
-	-	500, 300	1.20	1260, 1000	3.63	2160, 1000	3.95

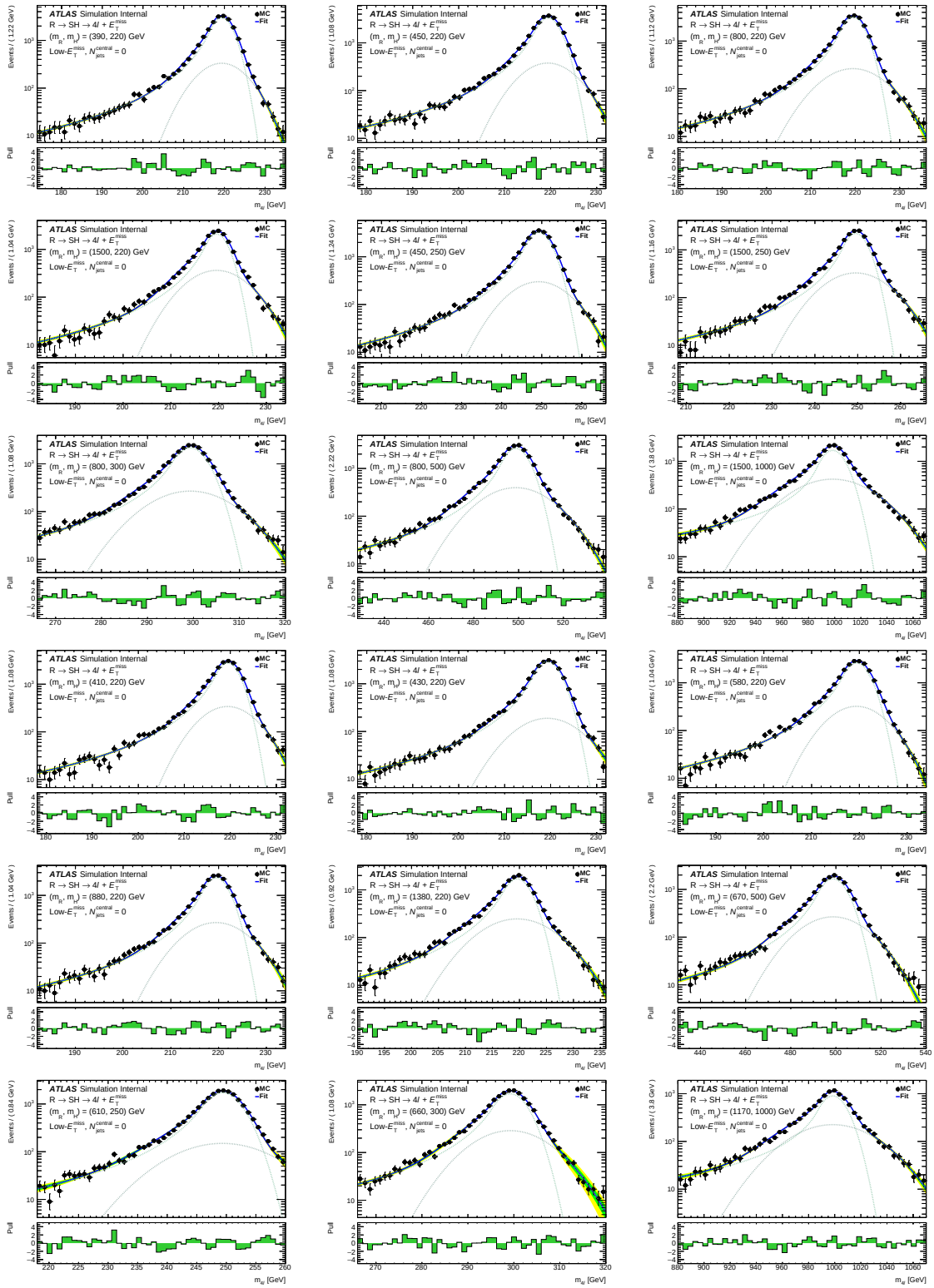

Figure 21: Distributions of the four-lepton invariant mass for fitting the $\mathcal{CB}+\mathcal{G}$ PDF of equation 6.1 to (390,220), (450,220), (800,220), (1500,220), (450,250), (1500,250), (800,300), (800,500), (1500,1000), (410,220), (430,220), (580,220), (880,220), (1380,220), (670,500), (610,250), (660,300) and (1170,1000) GeV signal mass points for the $R \rightarrow SH \rightarrow 4\ell + E_{\mathrm{T}}^{\mathrm{miss}}$ model. MC simulation of statistics equivalent to integrated luminosity of 139.0 fb^{-1}is used for the High-$E_{\mathrm{T}}^{\mathrm{miss}}$ and $N_{\mathrm{jets}}^{\mathrm{Central}} = 0$ category. The ratio plot in each figure shows the pull distribution.

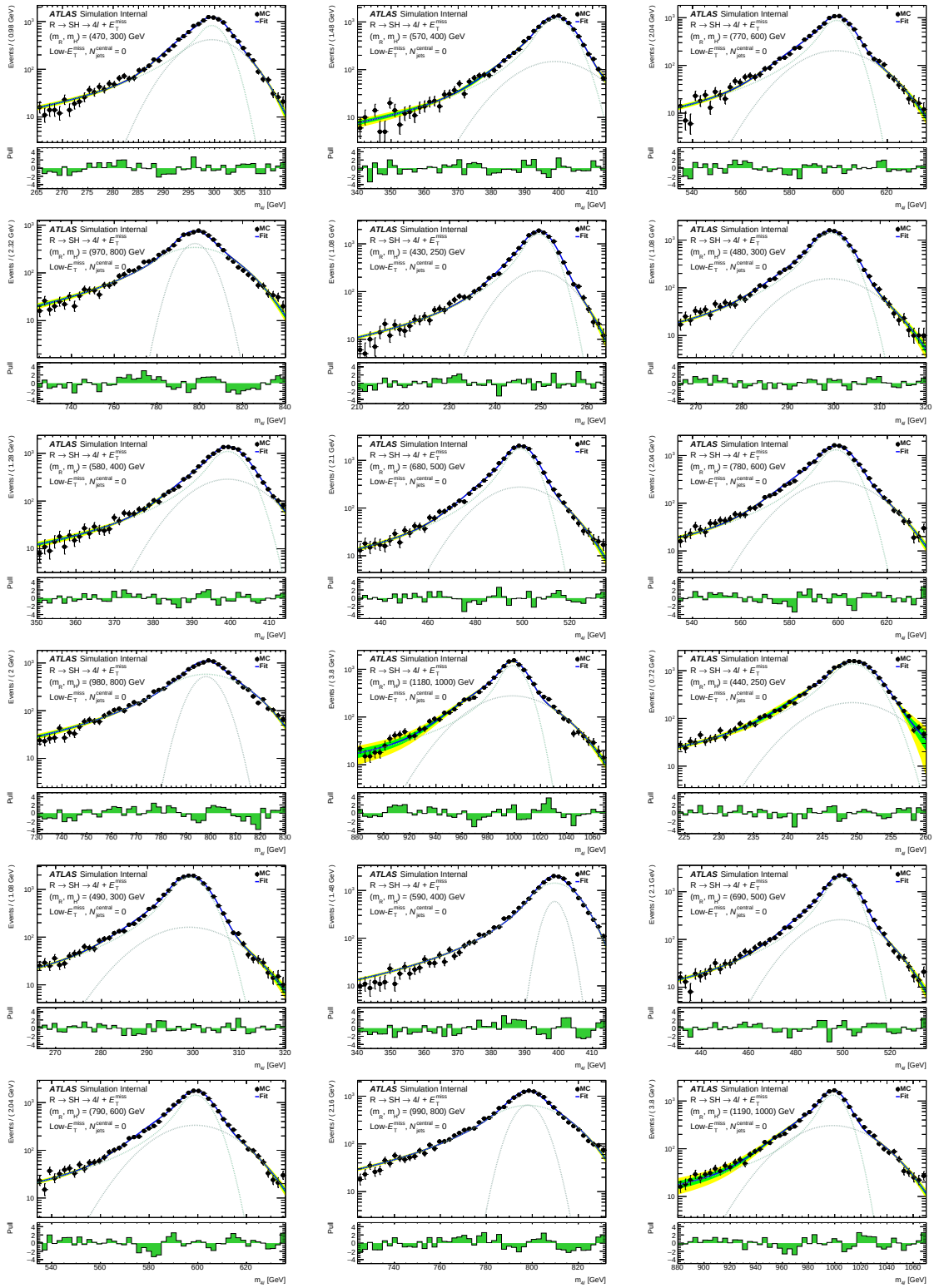

Figure 22: Distributions of the four-lepton invariant mass for fitting the $\mathcal{CB}+\mathcal{G}$ PDF of equation 6.1 to (470,300), (570,400), (770,600), (970,800), (430,250), (480,300), (580,400), (680,500), (780,600), (980,800), (1180,1000), (440,250), (490,300), (590,400), (690,500), (790,600), (990,800) and (1190,1000) GeV signal mass points for the $R \rightarrow SH \rightarrow 4\ell + E_{\mathrm{T}}^{\mathrm{miss}}$ model. MC simulation of statistics equivalent to integrated luminosity of 139.0 fb^{-1}is used for the High-$E_{\mathrm{T}}^{\mathrm{miss}}$ and $N_{\mathrm{jets}}^{\mathrm{Central}} = 0$ category. The ratio plot in each figure shows the pull distribution.

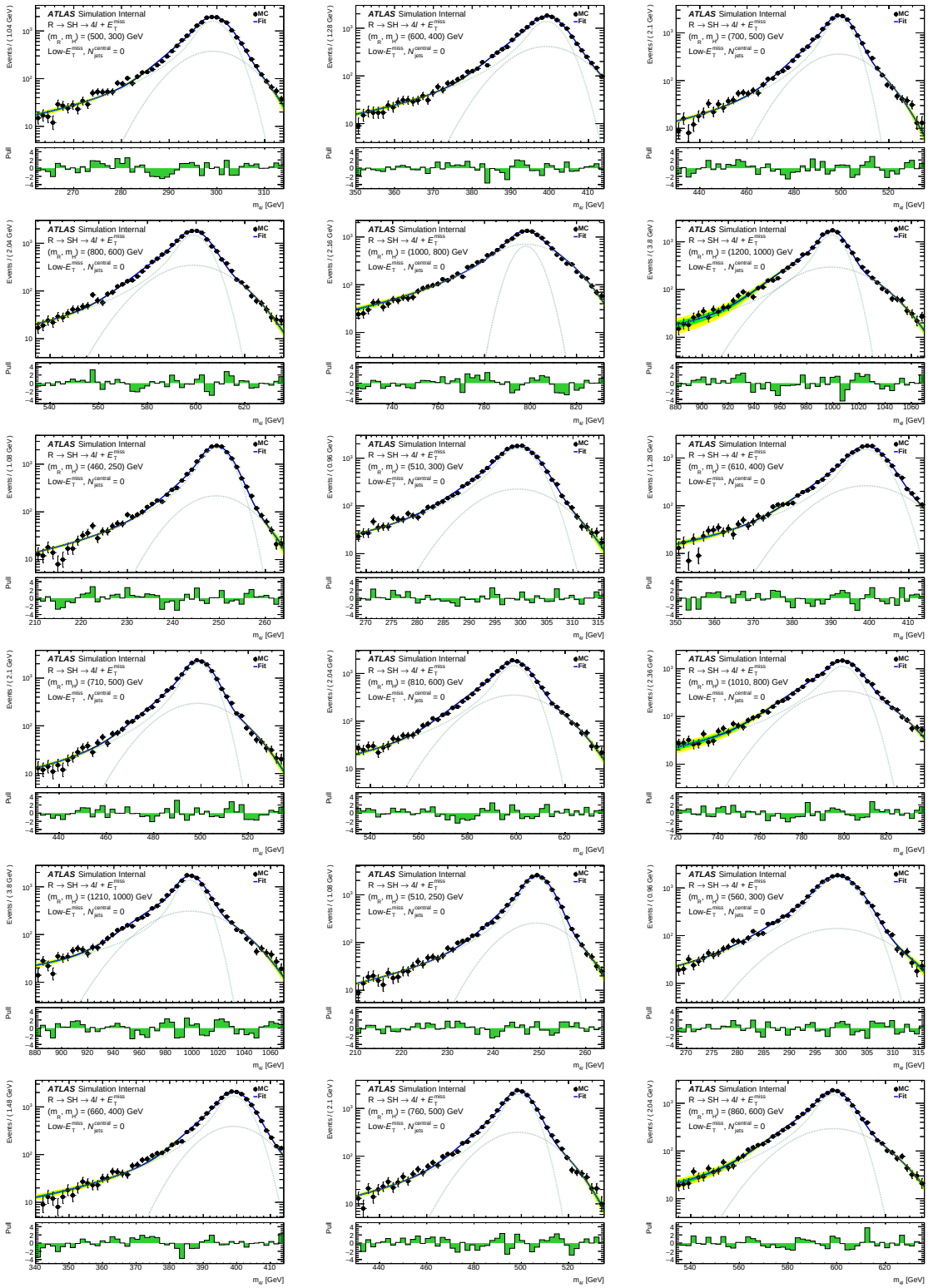

Figure 23: Distributions of the four-lepton invariant mass for fitting the $\mathcal{CB}+\mathcal{G}$ PDF of equation 6.1 to (500,300), (600,400), (800,600), (1000,800), (1000,800), (1200,1000), (460,250), (510,300), (610,400), (710,500), (810,600), (1010,800), (1210,1000), (510,250), (560,300), (660,400), (760,500) and (860,600) GeV signal mass points for the $R \rightarrow SH \rightarrow 4\ell + E_{\mathrm{T}}^{\mathrm{miss}}$ model. MC simulation of statistics equivalent to integrated luminosity of 139.0 fb^{-1}is used for the High-$E_{\mathrm{T}}^{\mathrm{miss}}$ and $N_{\mathrm{jets}}^{\mathrm{Central}} = 0$ category. The ratio plot in each figure shows the pull distribution.

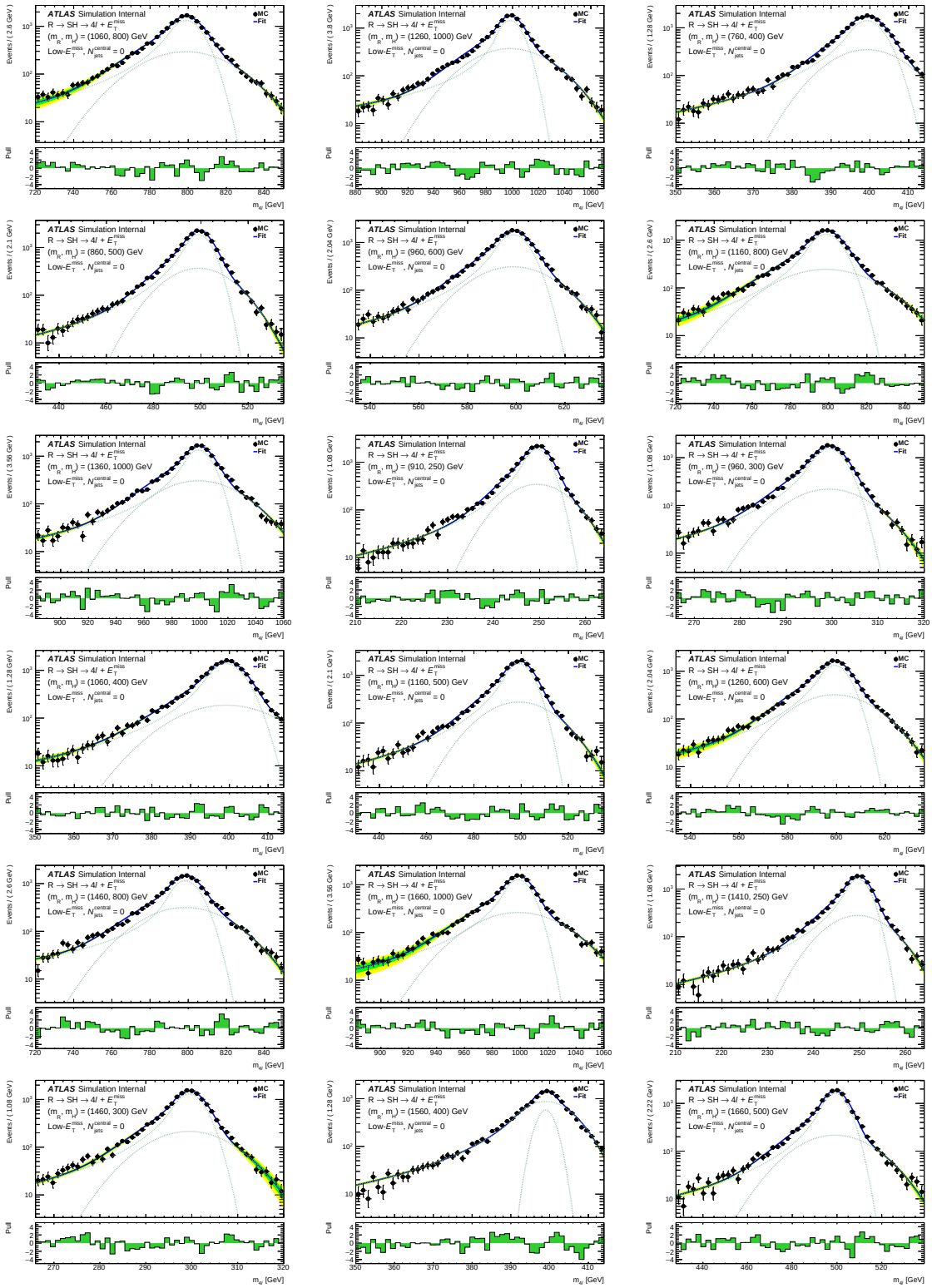

Figure 24: Distributions of the four-lepton invariant mass for fitting the $\mathcal{CB}+\mathcal{G}$ PDF of equation 6.1 to (1060,800), (1260,1000), (760,400), (860,500), (960,600), (1160,800), (1360,1000), (910,250), (960,300), (1060,400), (1160,500), (1260,600), (1460,800), (1660,1000), (1410,250), (1460,300), (1560,400) and (1660,500) GeV signal mass points for the $R \rightarrow SH \rightarrow 4\ell + E_{\mathrm{T}}^{\mathrm{miss}}$ model. MC simulation of statistics equivalent to integrated luminosity of 139.0 fb^{-1}is used for the High-$E_{\mathrm{T}}^{\mathrm{miss}}$ and $N_{\mathrm{jets}}^{\mathrm{Central}} = 0$ category. The ratio plot in each figure shows the pull distribution.

Table 8: Summary of χ^2/ndof values from fitting $\mathcal{CB}+\mathcal{G}$ PDF of equation 6.1 to different mass points of the $R \rightarrow SH \rightarrow 4\ell + E_{\mathrm{T}}^{\mathrm{miss}}$ model for the Low-$E_{\mathrm{T}}^{\mathrm{miss}}$ and $N_{\mathrm{jets}}^{\mathrm{Central}} \geq 1$ category. The χ^2/ndof are shown for Figures 31, 32, 33 and 34.

Mass point = (m_X, m_H) [GeV]	χ^2/ndof	Mass point = (m_X, m_H) [GeV]	χ^2/ndof	Mass point = (m_X, m_H) [GeV]	χ^2/ndof	Mass point = (m_X, m_H) [GeV]	χ^2/ndof
390, 220	2.72	470, 300	5.20	600, 400	2.62	760, 400	2.11
450, 220	2.89	570, 400	2.52	700, 500	4.11	860, 500	4.04
800, 220	3.13	770, 600	11.89	800, 600	2.96	960, 600	18.24
1500, 220	3.81	970, 800	8.10	1000, 800	6.69	1160, 800	4.39
450, 250	3.50	430, 250	6.72	1200, 1000	6.21	1360, 1000	42.13
1500, 250	4.11	480, 300	2.49	460, 250	2.24	910, 250	13.08
800, 300	2.93	580, 400	2.21	510, 300	2.08	960, 300	14.94
800, 500	3.95	680, 500	2.82	610, 400	2.29	1060, 400	2.79
1500, 1000	7.87	780, 600	2.93	710, 500	3.17	1160, 500	4.50
410, 220	2.47	980, 800	6.51	810, 600	13.04	1260, 600	12.18
430, 220	1.67	1180, 1000	4.85	1010, 800	2.73	1460, 800	3.46
580, 220	2.27	440, 250	3.90	1210, 1000	4.85	1660, 1000	10.40
880, 220	2.43	490, 300	27.01	510, 250	2.17	1410, 250	180.50
1380, 220	3.86	590, 400	5.04	560, 300	7.89	1460, 300	3.83
670, 500	3.37	690, 500	3.55	660, 400	2.16	1560, 400	6.35
610, 250	2.86	790, 600	4.21	760, 500	3.63	1660, 500	5.38
660, 300	3.45	990, 800	8.57	860, 600	4.04	1760, 600	5.24
1170, 1000	4.62	1190, 1000	4.76	1060, 800	3.94	1960, 800	3.60
-	-	500, 300	7.37	1260, 1000	5.59	2160, 1000	5.56

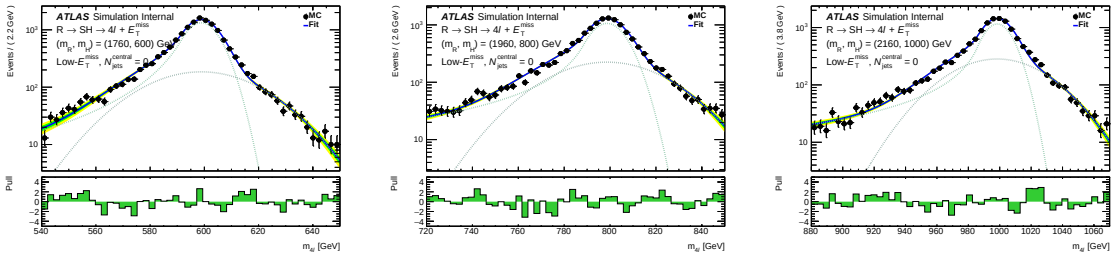

Figure 25: Distributions of the four-lepton invariant mass for fitting the $\mathcal{CB}+\mathcal{G}$ PDF of equation 6.1 to (1760,600), (1960,800) and (2160,1000) GeV signal mass points for the $R \rightarrow SH \rightarrow 4\ell + E_{\mathrm{T}}^{\mathrm{miss}}$ model. MC simulation of statistics equivalent to integrated luminosity of 139.0 fb^{-1} is used for the High-$E_{\mathrm{T}}^{\mathrm{miss}}$ and $N_{\mathrm{jets}}^{\mathrm{Central}} = 0$ category. The ratio plot in each figure shows the pull distribution.

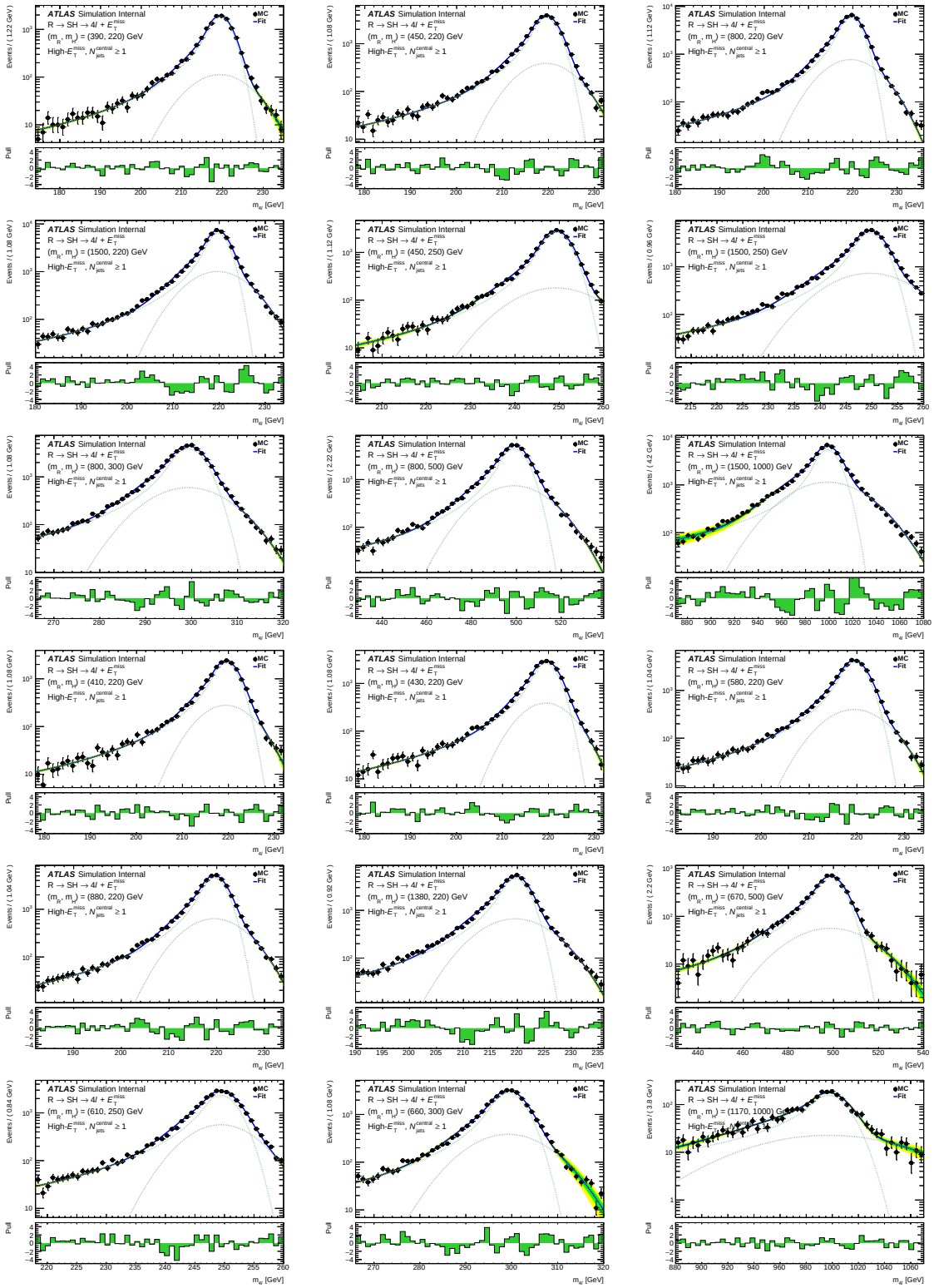

Figure 26: Distributions of the four-lepton invariant mass for fitting the $\mathcal{CB}+\mathcal{G}$ PDF of equation 6.1 to (390,220), (450,220), (800,220), (1500,220), (450,250), (1500,250), (800,300), (800,500), (1500,1000), (410,220), (430,220), (580,220), (880,220), (1380,220), (670,500), (610,250), (660,300) and (1170,1000) GeV signal mass points for the $R \rightarrow SH \rightarrow 4\ell + E_{\mathrm{T}}^{\mathrm{miss}}$ model. MC simulation of statistics equivalent to integrated luminosity of 139.0 fb^{-1}is used for the High-$E_{\mathrm{T}}^{\mathrm{miss}}$ and $N_{\mathrm{jets}}^{\mathrm{Central}} \geq 1$ category. The ratio plot in each figure shows the pull distribution.

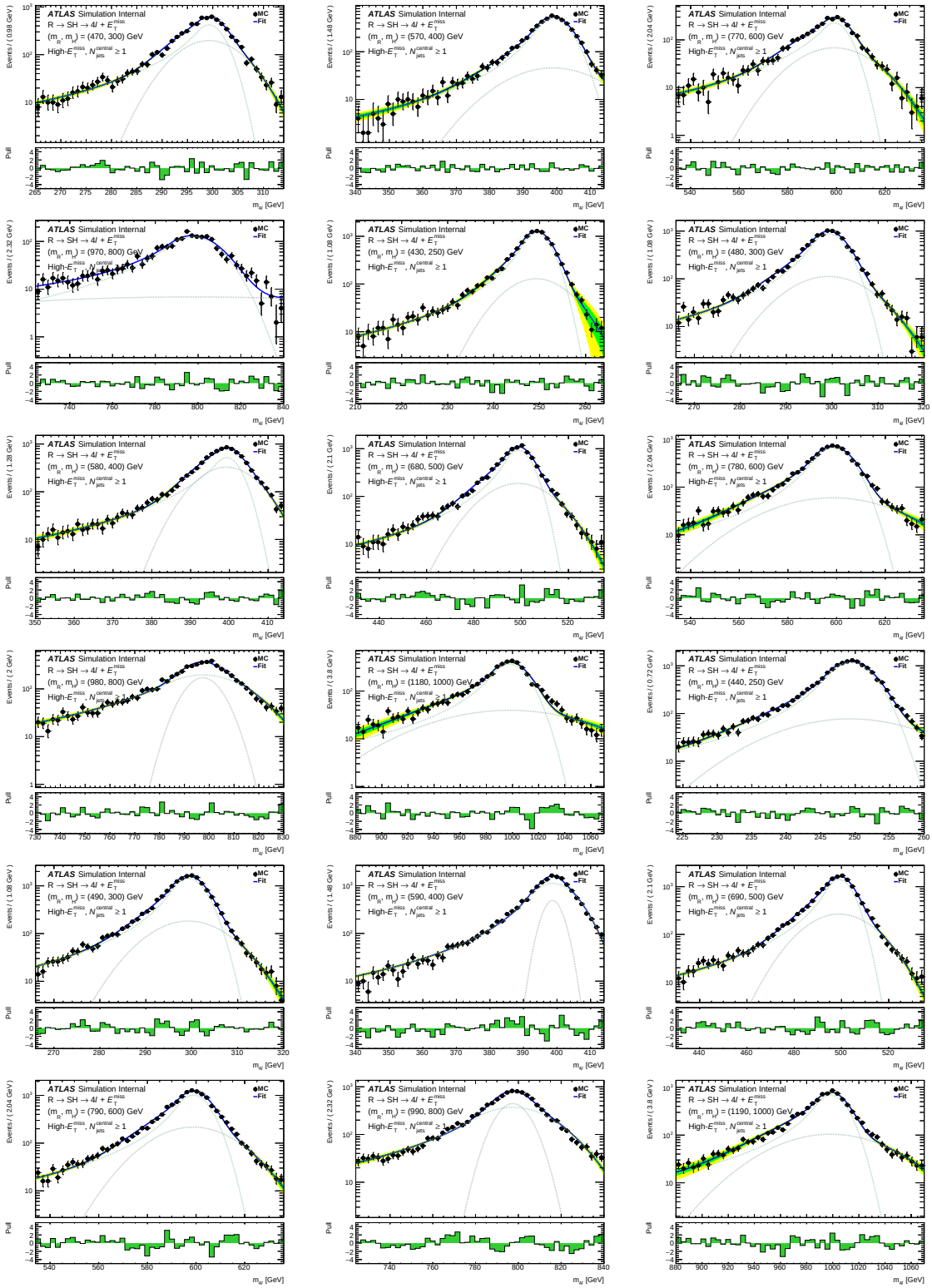

Figure 27: Distributions of the four-lepton invariant mass for fitting the $\mathcal{CB}+\mathcal{G}$ PDF of equation 6.1 to (470,300), (570,400), (770,600), (970,800), (430,250), (480,300), (580,400), (680,500), (780,600), (980,800), (1180,1000), (440,250), (490,300), (590,400), (690,500), (790,600), (990,800) and (1190,1000) GeV signal mass points for the $R \rightarrow SH \rightarrow 4\ell + E_{\mathrm{T}}^{\mathrm{miss}}$ model. MC simulation of statistics equivalent to integrated luminosity of 139.0 fb^{-1}is used for the High-$E_{\mathrm{T}}^{\mathrm{miss}}$ and $N_{\mathrm{jets}}^{\mathrm{Central}} \geq 1$ category. The ratio plot in each figure shows the pull distribution.

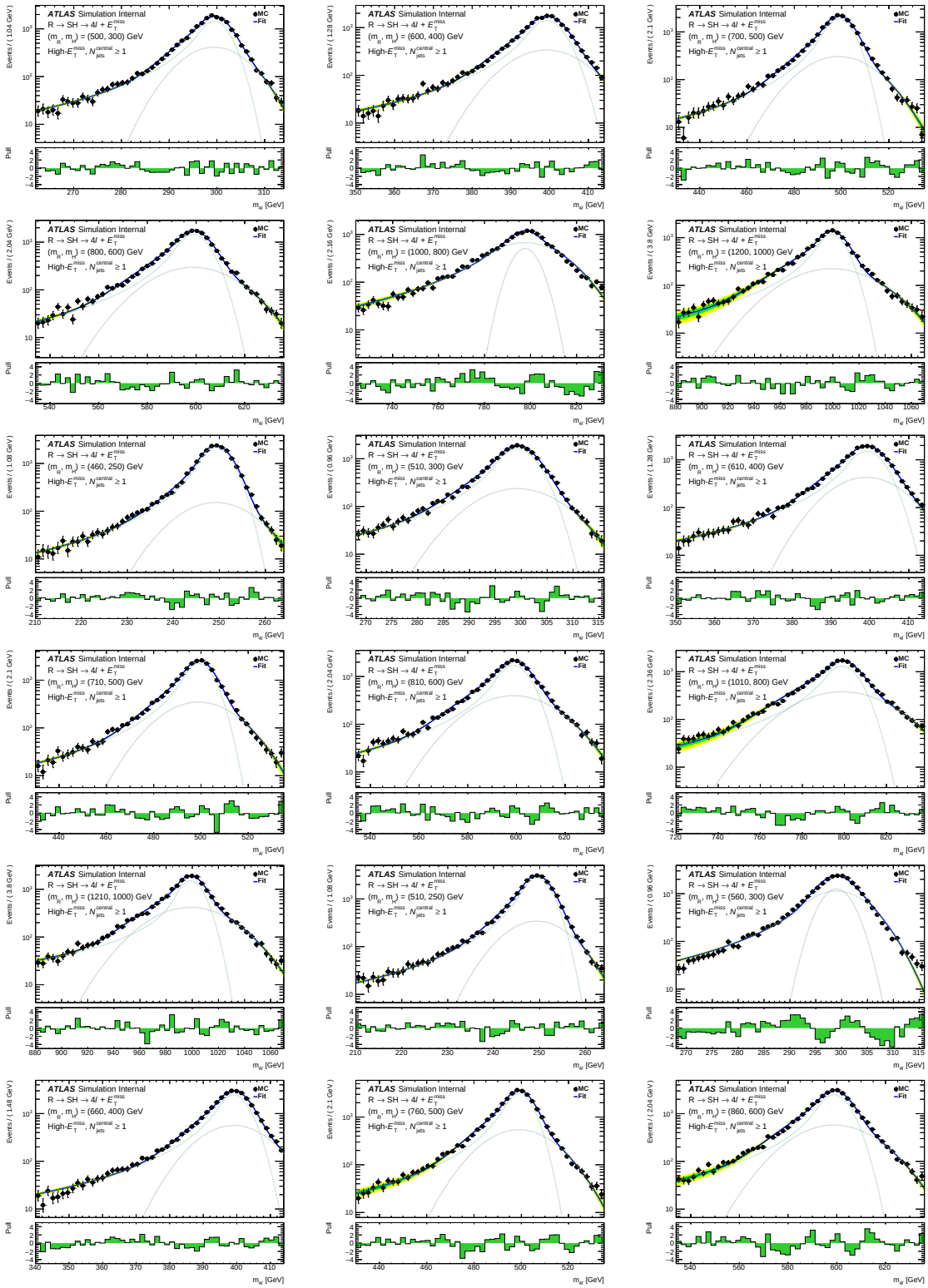

Figure 28: Distributions of the four-lepton invariant mass for fitting the $\mathcal{CB}+\mathcal{G}$ PDF of equation 6.1 to (500,300), (600,400), (800,600), (1000,800), (1000,800), (1200,1000), (460,250), (510,300), (610,400), (710,500), (810,600), (1010,800), (1210,1000), (510,250), (560,300), (660,400), (760,500) and (860,600) GeV signal mass points for the $R \rightarrow SH \rightarrow 4\ell + E_{\mathrm{T}}^{\mathrm{miss}}$ model. MC simulation of statistics equivalent to integrated luminosity of 139.0 fb^{-1}is used for the High-$E_{\mathrm{T}}^{\mathrm{miss}}$ and $N_{\mathrm{jets}}^{\mathrm{Central}} \geq 1$ category. The ratio plot in each figure shows the pull distribution.

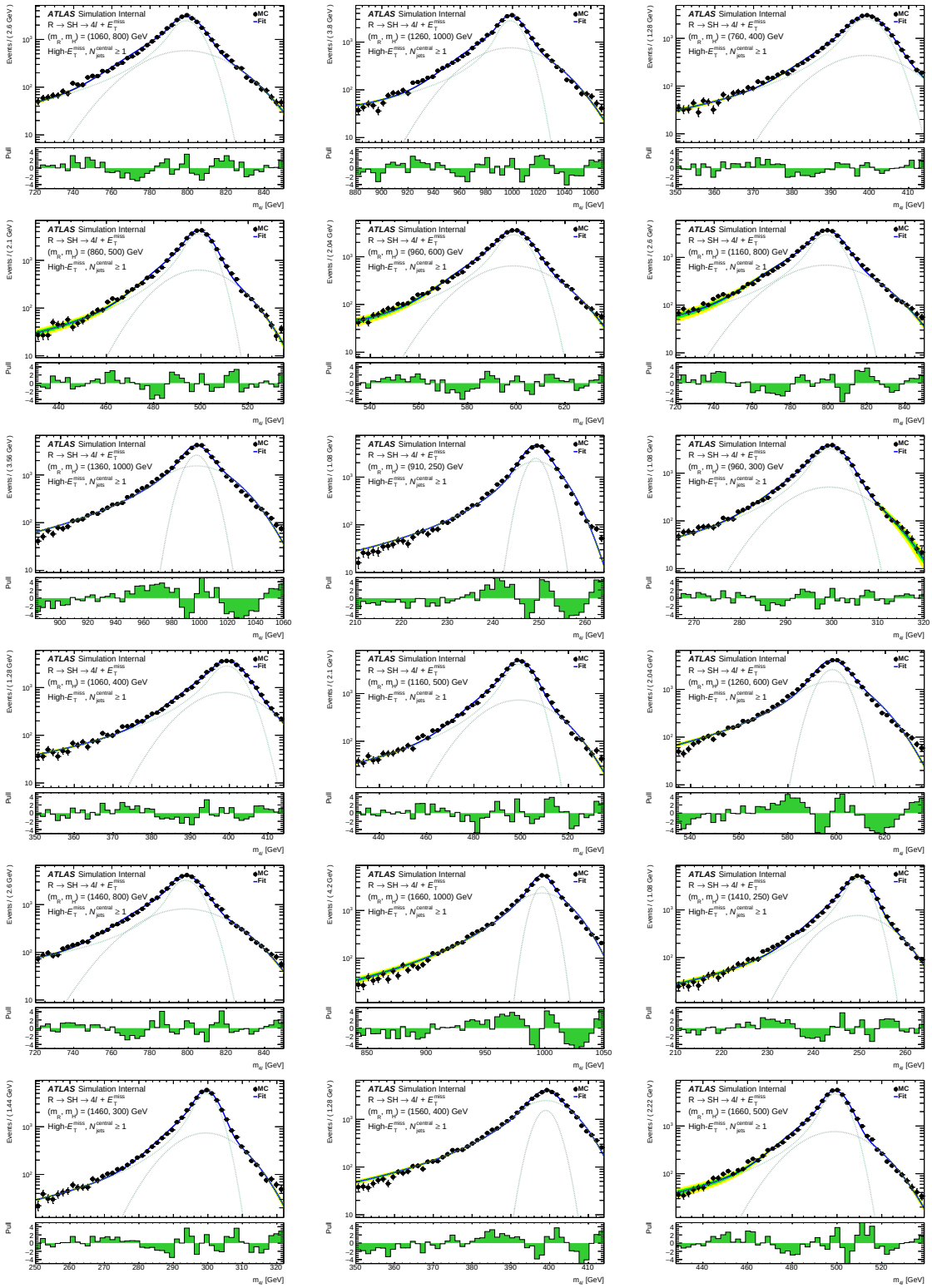

Figure 29: Distributions of the four-lepton invariant mass for fitting the $\mathcal{CB}+\mathcal{G}$ PDF of equation 6.1 to (1060,800), (1260,1000), (760,400), (860,500), (960,600), (1160,800), (1360,1000), (910,250), (960,300), (1060,400), (1160,500), (1260,600), (1460,800), (1660,1000), (1410,250), (1460,300), (1560,400) and (1660,500) GeV signal mass points for the $R \rightarrow SH \rightarrow 4\ell + E_{\mathrm{T}}^{\mathrm{miss}}$ model. MC simulation of statistics equivalent to integrated luminosity of 139.0 fb^{-1}is used for the High-$E_{\mathrm{T}}^{\mathrm{miss}}$ and $N_{\mathrm{jets}}^{\mathrm{Central}} \geq 1$ category. The ratio plot in each figure shows the pull distribution.

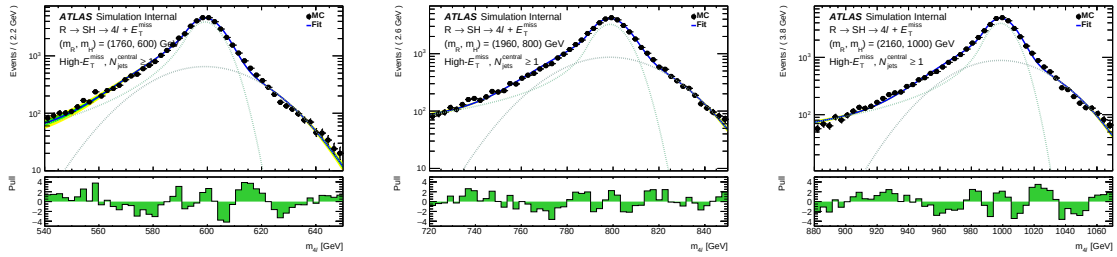

Figure 30: Distributions of the four-lepton invariant mass for fitting the $\mathcal{CB} + \mathcal{G}$ PDF of equation 6.1 to (1760,600), (1960,800) and (2160,1000) GeV signal mass points for the $R \rightarrow SH \rightarrow 4\ell + E_{\mathrm{T}}^{\mathrm{miss}}$ model. MC simulation of statistics equivalent to integrated luminosity of 139.0 fb^{-1}is used for the High-$E_{\mathrm{T}}^{\mathrm{miss}}$ and $N_{\mathrm{jets}}^{\mathrm{Central}} \geq 1$ category. The ratio plot in each figure shows the pull distribution.

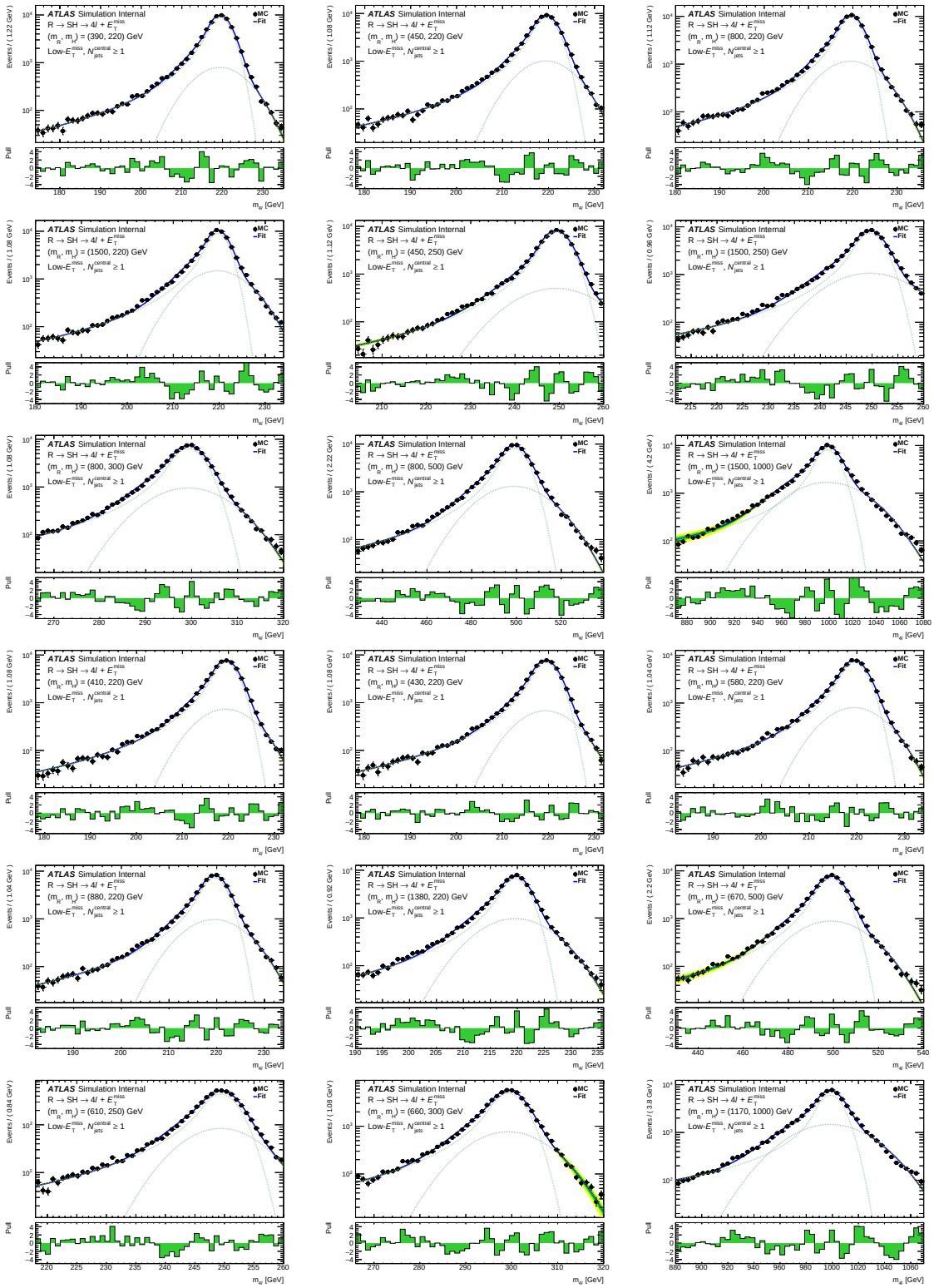

Figure 31: Distributions of the four-lepton invariant mass for fitting the $\mathcal{CB}+\mathcal{G}$ PDF of equation 6.1 to (390,220), (450,220), (800,220), (1500,220), (450,250), (1500,250), (800,300), (800,500), (1500,1000), (410,220), (430,220), (580,220), (880,220), (1380,220), (670,500), (610,250), (660,300) and (1170,1000) GeV signal mass points for the $R \rightarrow SH \rightarrow 4\ell + E_{\mathrm{T}}^{\mathrm{miss}}$ model. MC simulation of statistics equivalent to integrated luminosity of 139.0 fb^{-1}is used for the Low-$E_{\mathrm{T}}^{\mathrm{miss}}$ and $N_{\mathrm{jets}}^{\mathrm{Central}} \geq 1$ category. The ratio plot in each figure shows the pull distribution.

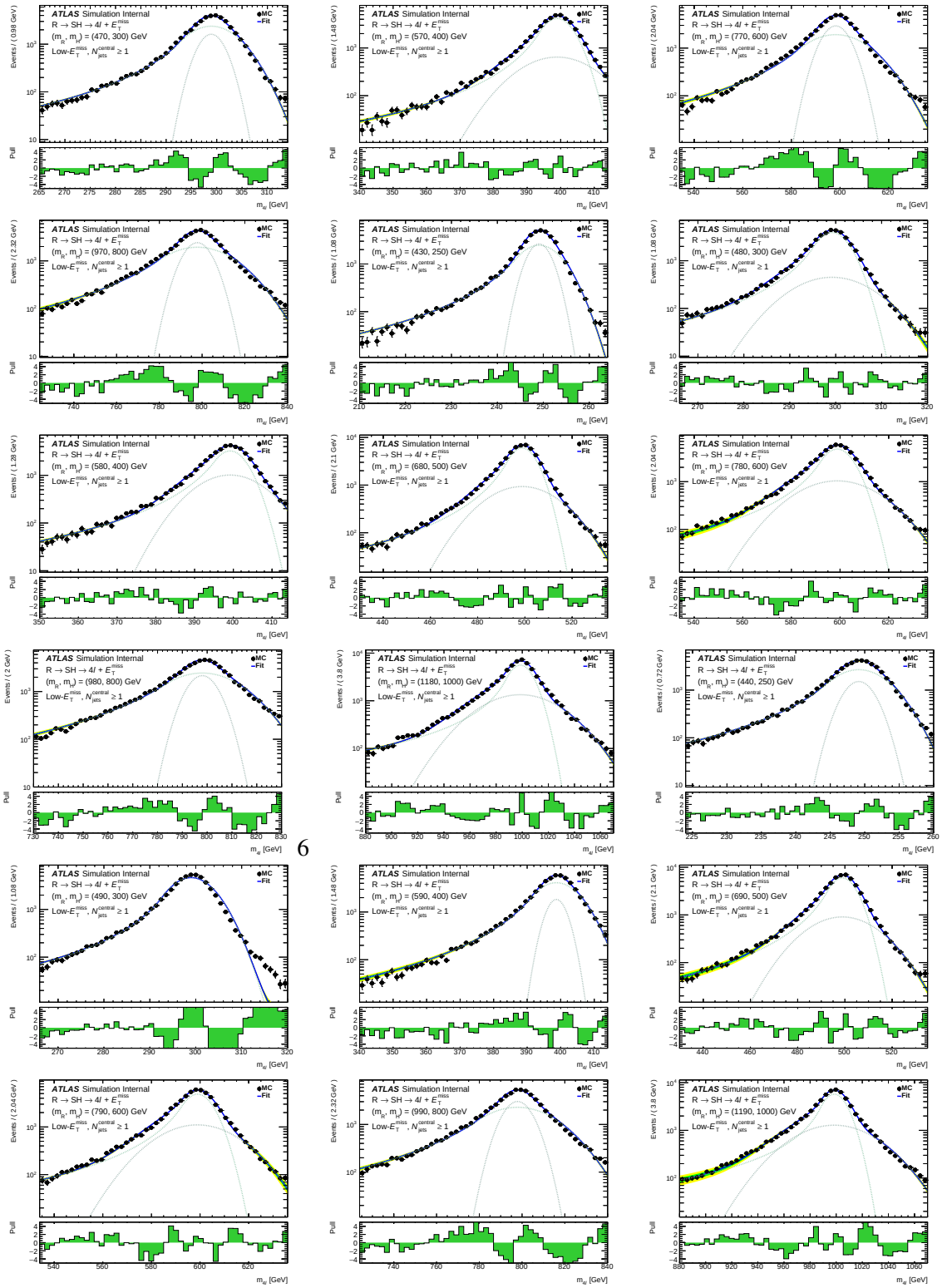

Figure 32: Distributions of the four-lepton invariant mass for fitting the $\mathcal{CB}+\mathcal{G}$ PDF of equation 6.1 to (470,300), (570,400), (770,600), (970,800), (430,250), (480,300), (580,400), (680,500), (780,600), (980,800), (1180,1000), (440,250), (490,300), (590,400), (690,500), (790,600), (990,800) and (1190,1000) GeV signal mass points for the $R \rightarrow SH \rightarrow 4\ell + E_{\mathrm{T}}^{\mathrm{miss}}$ model. MC simulation of statistics equivalent to integrated luminosity of 139.0 fb^{-1}is used for the Low-$E_{\mathrm{T}}^{\mathrm{miss}}$ and $N_{\mathrm{jets}}^{\mathrm{Central}} \geq 1$ category. The ratio plot in each figure shows the pull distribution.

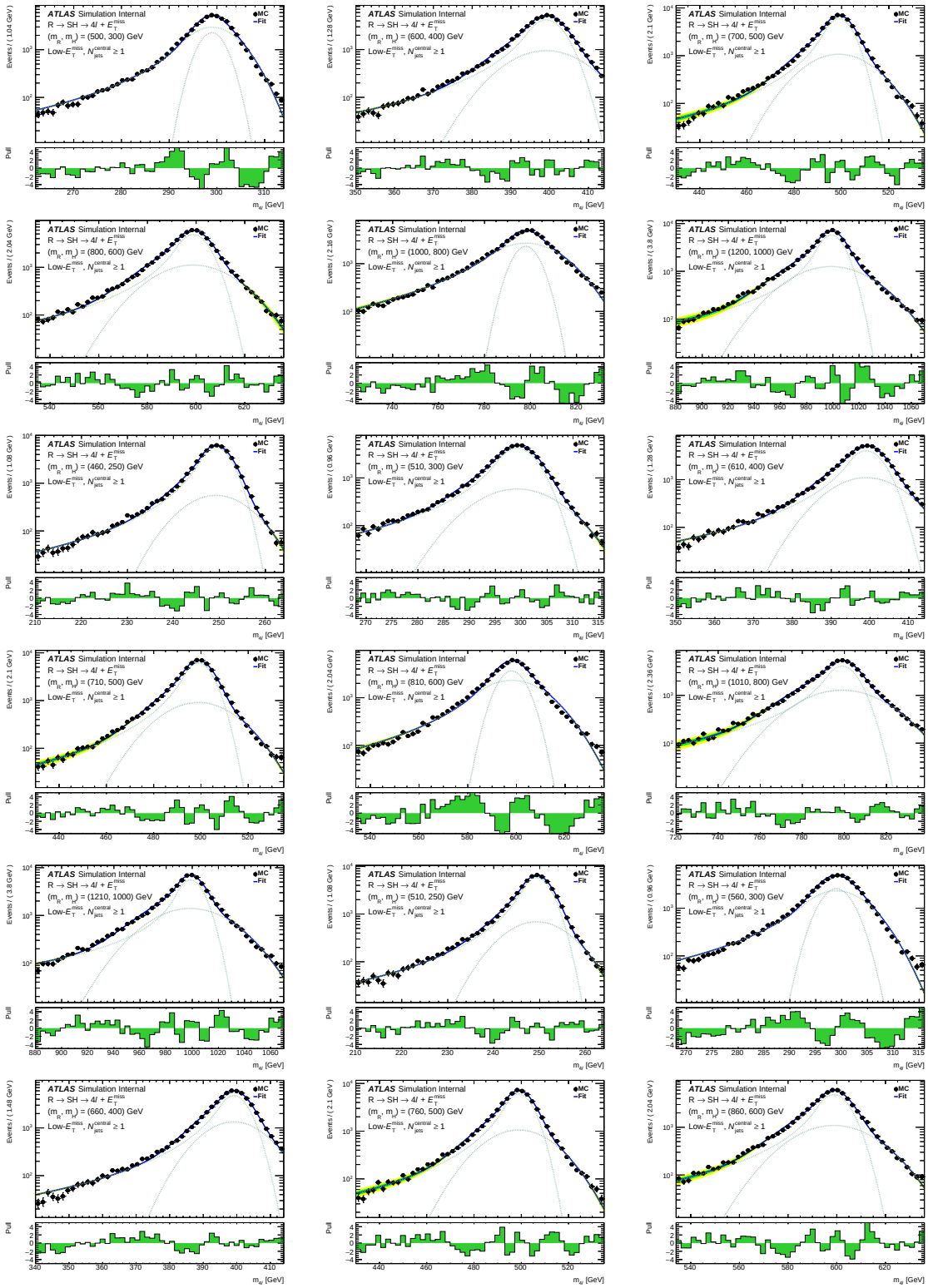

Figure 33: Distributions of the four-lepton invariant mass for fitting the $\mathcal{CB}+\mathcal{G}$ PDF of equation 6.1 to (500,300), (600,400), (800,600), (1000,800), (1000,800), (1200,1000), (460,250), (510,300), (610,400), (710,500), (810,600), (1010,800), (1210,1000), (510,250), (560,300), (660,400), (760,500) and (860,600) GeV signal mass points for the $R \rightarrow SH \rightarrow 4\ell + E_{\mathrm{T}}^{\mathrm{miss}}$ model. MC simulation of statistics equivalent to integrated luminosity of 139.0 fb^{-1}is used for the Low-$E_{\mathrm{T}}^{\mathrm{miss}}$ and $N_{\mathrm{jets}}^{\mathrm{Central}} \geq 1$ category. The ratio plot in each figure shows the pull distribution.

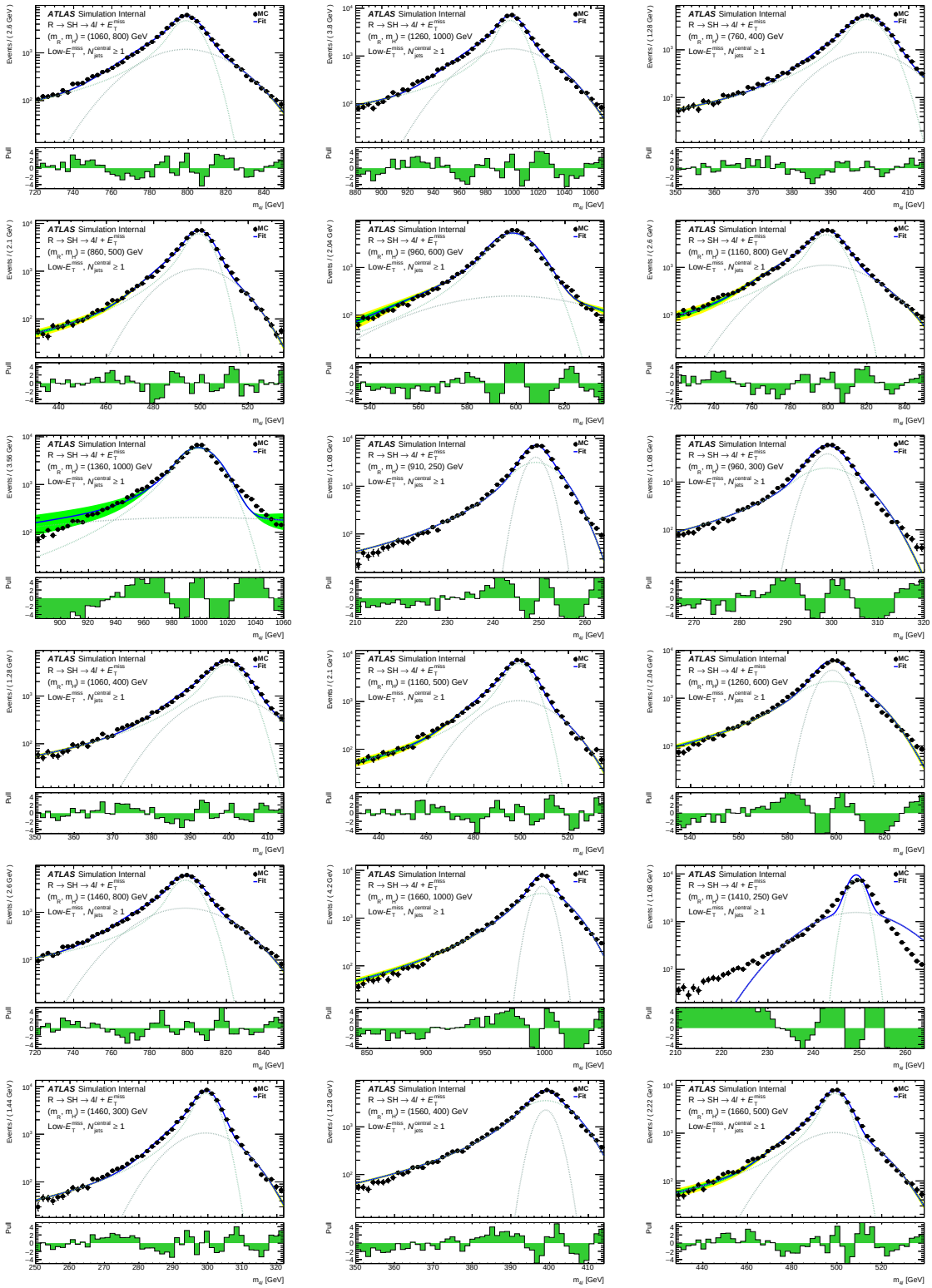

Figure 34: Distributions of the four-lepton invariant mass for fitting the $\mathcal{CB}+\mathcal{G}$ PDF of equation 6.1 to (1060,800), (1260,1000), (760,400), (860,500), (960,600), (1160,800), (1360,1000), (910,250), (960,300), (1060,400), (1160,500), (1260,600), (1460,800), (1660,1000), (1410,250), (1460,300), (1560,400) and (1660,500) GeV signal mass points for the $R \rightarrow SH \rightarrow 4\ell + E_{\mathrm{T}}^{\mathrm{miss}}$ model. MC simulation of statistics equivalent to integrated luminosity of 139.0 fb^{-1}is used for the Low-$E_{\mathrm{T}}^{\mathrm{miss}}$ and $N_{\mathrm{jets}}^{\mathrm{Central}} \geq 1$ category. The ratio plot in each figure shows the pull distribution.

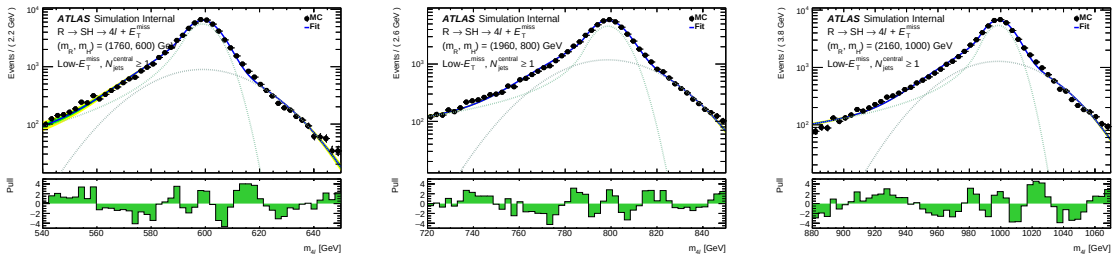

Figure 35: Distributions of the four-lepton invariant mass for fitting the $\mathcal{CB} + \mathcal{G}$ PDF of equation 6.1 to (1760,600), (1960,800) and (2160,1000) GeV signal mass points for the $R \rightarrow SH \rightarrow 4\ell + E_{\mathrm{T}}^{\mathrm{miss}}$ model. MC simulation of statistics equivalent to integrated luminosity of 139.0 fb^{-1}is used for the Low-$E_{\mathrm{T}}^{\mathrm{miss}}$ and $N_{\mathrm{jets}}^{\mathrm{Central}} \geq 1$ category. The ratio plot in each figure shows the pull distribution.

B $E_{\mathrm{T}}^{\mathrm{miss}}$ performance

All plots here need to be fixed. For instance, adding ratio plots, taking care of the style and checking the units. Then add text to explain what is going on here.

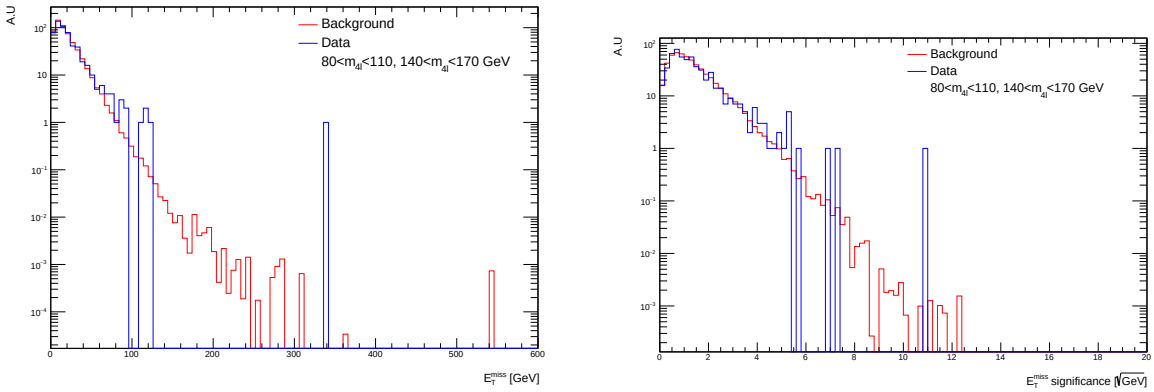

(a) (b)

Figure 36: Distribution of the (a) Missing transverse energy and (a) $E_{\mathrm{T}}^{\mathrm{miss}}$ significance at a control region of $80 < m_{4\ell} < 110$ GeV and $140 < m_{4\ell} < 170$ GeVfor the High-$E_{\mathrm{T}}^{\mathrm{miss}}$ and $N_{\mathrm{jets}}^{\mathrm{Central}} = 0$ category at 139.0 fb^{-1}.

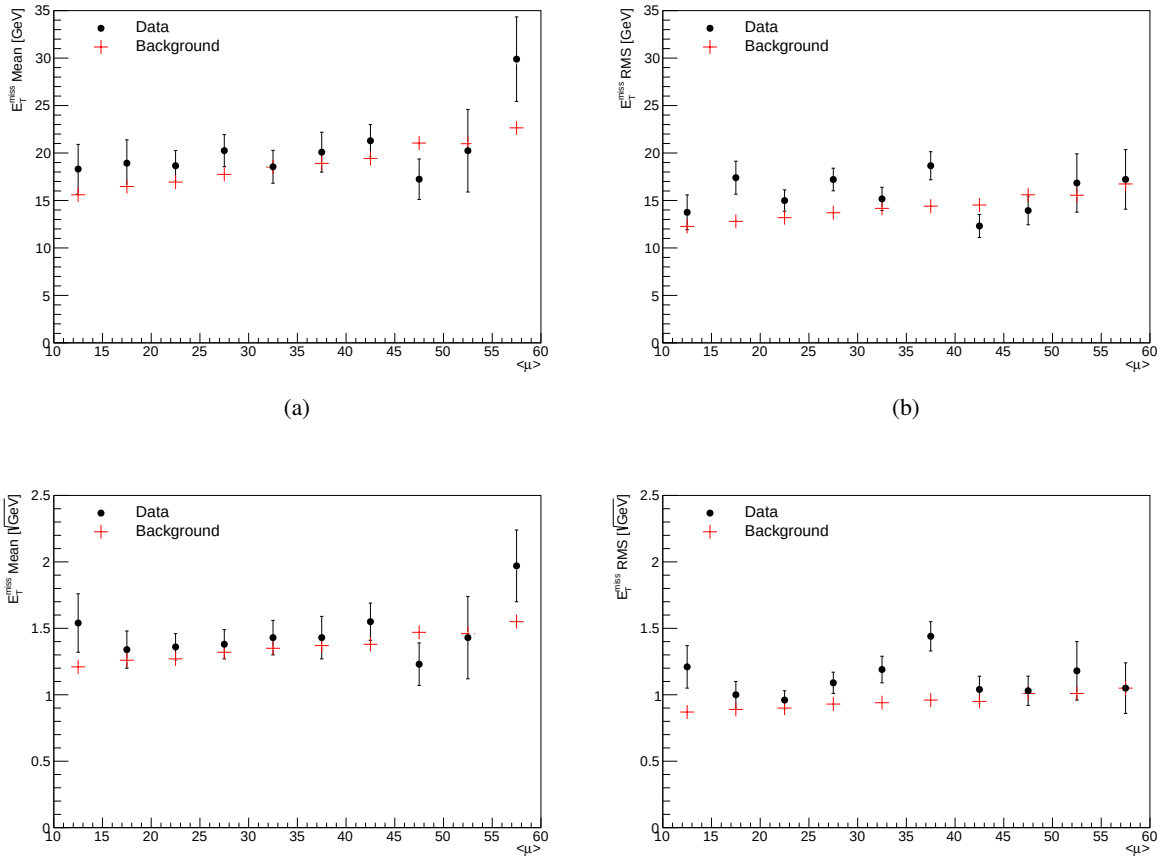
Data
Background
E_T^{miss} Mean [GeV]
E_T^{miss} RMS [GeV]
E_T^{miss} Mean [$\sqrt{GeV}$]
E_T^{miss} RMS [$\sqrt{GeV}$]
<μ>
(a)
(b)
(c)
(d)

Figure 37